Phase transitions of rare earth oxide films grown on Si(111)

Dissertation (kumulativ)

zur Erlangung des Grades eines
Doktors der Naturwissenschaften (Dr. rer. nat.)

dem Fachbereich Physik der Universität Osnabrück
vorgelegt von

Henrik Wilkens, Dipl. Phys.

Osnabrück, Januar 2014

Contents

1 Introduction

Rare earth oxides (REOs) show unique material properties such as high dielectric constants [1,2] or high oxygen mobilities [3] and are in focus of several research fields. A large number of applications can be found ranging from microelectronics [4] and optical technologies [5,6] to catalysis [7].

The most common electronic devices are silicon based metal-oxide-semiconductor (MOS) field effect transistors (FETs) (cf. Fig. 1.1). One of the reasons for the great success of the silicon technology is the ongoing improvement of performance by scaling down the transistor size. The number of transistors more or less doubles in two or three year periods according to Moore's law [8]. The limiting factor of the scaling process is the gate dielectric in MOSFET devices. Since the 1970s the native silicon oxide SiO_2 has been used for this purpose due to its high thermal and chemical stability. However, scaling the SiO_2 layer below ≈ 2 nm results in bad device performance due to high leakage currents based on quantum mechanical tunneling and loss of bulk electronic properties [9,10]. Therefore, new concepts are needed to overcome this scaling limit.
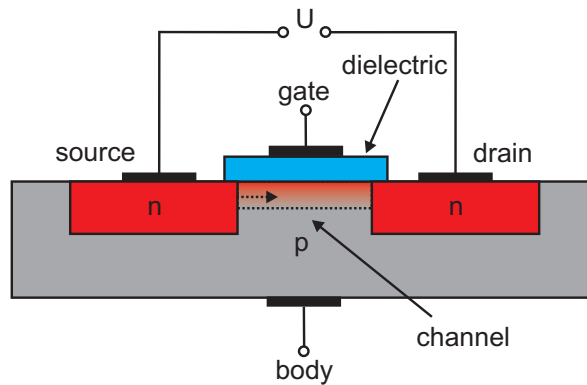
Figure 1.1: Sketch of a n-channel MOSFET device. Two heavily n-doped regions are embedded in p-doped substrate. The gate contact is separated from the substrate by the gate dielectric forming a capacitor. By applying a voltage between body and gate, electrons from the substrate are drawn to the interface of the dielectric. At the interface the electrons recombine with holes which are the major charge carriers of the substrate. If a certain threshold voltage is overcome, an inversion layer with high electron concentration called n-channel will be formed and the circuit between source and drain will be closed.

One approach is the replacement of the gate oxide by materials with high dielectric constants (high k). These materials offer the same transistor performance as SiO_2 at thinner layer thicknesses. The number of suitable candidates is limited by their physical and chemical properties, e. g. thermal stability or low bulk defect density [11]. Several REOs fulfill the requirements and the integration of these films on the silicon platform is currently investigated [12–16].

Another important application of the REOs is catalysis where they are used as a direct cat-

alyst [17–19] or as a support system for metal catalysts [20–22]. The catalytic reactivity and selectivity of the REOs is strongly influenced by their structural properties, e.g. surface morphology or density of oxygen vacancies. In addition, the complex phase diagrams, especially of the binary rare earth oxides [23], make it quite challenging to understand the catalytic reactions in detail.

Here, thin film systems, which can be used as a model catalyst [24–26], offer a great opportunity to get deeper insight on catalysis on an atomic scale. First of all, thin film systems can be prepared and studied under ultra high vacuum (UHV) conditions which offer a highly controllable environment and give access to several surface science techniques. Furthermore, the structural complexity is reduced since more or less two dimensional objects are investigated. In addition, complex polycrystalline structures can be simplified by epitaxial growth of single crystalline films with well defined crystallographic orientations.

Before these systems can be used as gate dielectric or in model catalyst experiments, a full characterization of their surface and bulk structure is necessary. In this work epitaxial films of the rare earth oxides praseodymia and ceria grown on Si(111) substrates are investigated. Furthermore, the thermal stability of the rare earth oxide films needs to be explored since undesired silicides and silicates maybe form at elevated temperatures [27–30]. The investigations presented in this work address these tasks.

In Chapter 2 a short theoretical overview of bulk and surface crystal structures is given. Furthermore, the theoretical basics of the used experimental techniques are described. Afterward, in Chapter 3 the investigated materials are introduced. The sample preparation as well as details of the experimental setups can be found in Chapter 4.

The results of this thesis were published in several scientific journals and are cumulatively presented in the Chapters 5 - 8. The investigation of the surface structure of hex-Pr_2O_3(0001) films grown on Si(111) as well as the evaluation of amorphous germanium capping layers is presented in Chapter 5. A combined thermal programmed desorption (TPD) and x-ray diffraction (XRD) study of the reduction process of plasma oxidized PrO_2(111) films can be found in Chapter 6.

In Chapter 7 it is shown that the Ce_7O_{12} surface structure of ceria can be stabilized by thermal reduction of a CeO_2(111)/hex-Pr_2O_3(0001)/Si(111) system. A detailed post deposition annealing (PDA) study of this system addressing the surface and bulk properties is presented in Chapter 8.

Chapter 9 summarizes the important results obtained in this thesis and gives an outlook for future experiments.

2 Theoretical background

In this chapter the theoretical concepts relevant for this thesis are introduced. First an introduction of crystal structures is given. Afterward the theory of the used x-ray and electron diffraction techniques is described. In the last part of this chapter the theory of the spectroscopic methods are briefly presented.

2.1 Crystal structures

In this thesis the structural properties of crystalline thin films are investigated. Therefore, a brief introduction of the existing crystal structures and their classification is presented in this section. A detailed description can be found in Refs. [31–33].
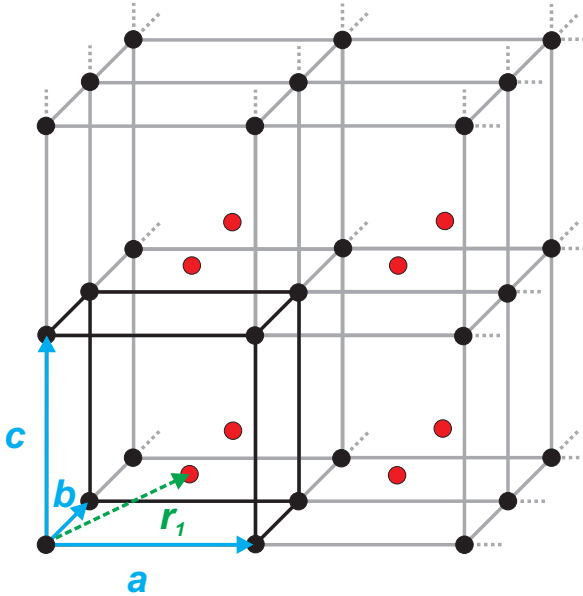
Figure 2.1: Example of a cubic unit cell with biatomic basis: The cubic unit cell is defined by the lattice vectors $\boldsymbol{a}$, $\boldsymbol{b}$ and $\boldsymbol{c}$. The position of the second atom inside the unit cell is given by the vector $\boldsymbol{r_1}$.

2.1.1 Bulk structures

An ideal crystal is a periodic arrangement of atoms infinitely repeated in all spatial directions. Based on this periodic nature only one repeating unit has to be considered to describe the entire system. This unit cell is spanned by three linear independent vectors $\boldsymbol{a}$, $\boldsymbol{b}$ and $\boldsymbol{c}$. The crystal lattice is formed by the translation of the unit cell via the operation

$$\boldsymbol{T} = u\boldsymbol{a} + v\boldsymbol{b} + w\boldsymbol{c} \quad \text{with} \quad u, v, w \in \mathbb{Z}\,. \tag{2.1}$$

Note, the size and shape of a unit cell can be chosen quite arbitrarily since only the translation symmetry has to be considered. Therefore, it is possible to define several unit cells describing the same crystal structure. The smallest possible unit cell is called primitive unit cell.

An additional coordinate system with the origin at one corner of the unit cell is used to express the position of the atoms within the unit cell. The vectors $\boldsymbol{r_i}$ (i= 1, 2, 3 ...) defining

these positions combined with atomic species are called atomic basis (cf. Fig. 2.1). The entire crystalline structure can be described by a combination of the atomic basis and the crystal lattice.

Bravais demonstrated by the evaluation of possible symmetry axes and inversion operations that only 14 types of crystal lattices exist [34]. Based on their symmetry properties these so called Bravais lattices can be assigned to seven crystal systems (triclinic, monoclinic, orthorombic, tetragonal, rhombohedral, hexagonal, cubic). A detailed description of all Bravais lattices can be found in Ref. [32].

2.1.2 Lattice planes

Lattice planes within crystal systems are commonly described by three integer values h, k and l denoted as (hkl). These so called Miller indices [35] can be obtained by the intersection points of a lattice plane with the three crystal axis at a/h, b/k and c/l. If any of the values is not an integer, the whole tuple is multiplied by the smallest common integer multiple. Negative values are denoted with a bar, e.g. -2 becomes $\bar{2}$, and if a plane does not intersect a crystal axis the corresponding Miller index is zero. The notation $[uvw]$ is used for direction using the basis given by the lattice vectors (cf. Fig. 2.2 (a)).
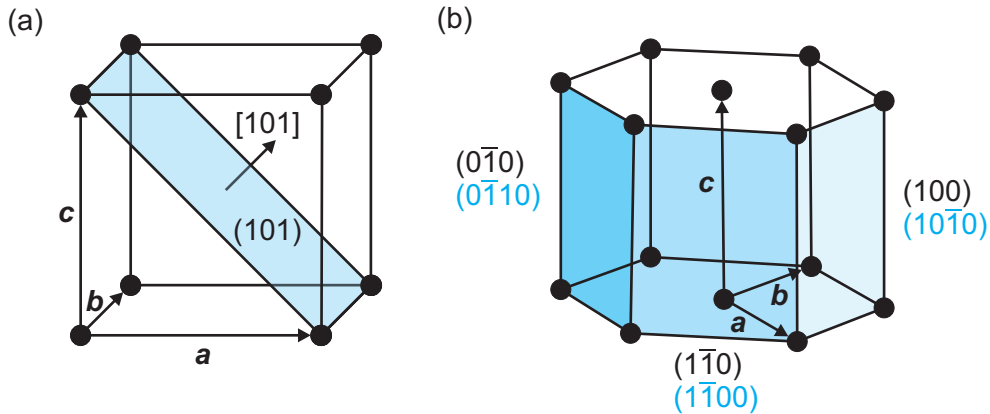
Figure 2.2: (a) Example of the Miller notation for a simple cubic system. The (101) plane intersects the crystal axis $\boldsymbol{a}$ and $\boldsymbol{c}$ at multiple of one. (b) Hexagonal crystal structure: Equivalent planes are given in the conventional Miller notation (black) and in the four index variant (blue).

All equivalent planes and directions in terms of symmetry are given by $\{hkl\}$ and $\langle uvw \rangle$, respectively.

Often, for the description of hexagonal systems a fourth redundant Miller index i is used. The index is given by $i = -(h + k)$ and lattice planes are denoted by $(hkil)$. This notation is convenient since equivalent planes can be described by index permutation, e.g. $(0\bar{1}10) \cong (1\bar{1}00) \cong (10\bar{1}0)$ etc. (cf. Fig. 2.2 (b)).

2.1.3   Surface structures

In reality crystals with infinite spatial expansion do not exist. Therefore, the reduced translation symmetry at the surfaces has to be considered. The surface of a crystal can be described as a two dimensional lattice with the translation vector

$$\boldsymbol{T} = u\boldsymbol{a} + v\boldsymbol{b} \quad \text{with} \quad u, v \in \mathbb{Z} \tag{2.2}$$

reducing the number of Bravais lattices to five.
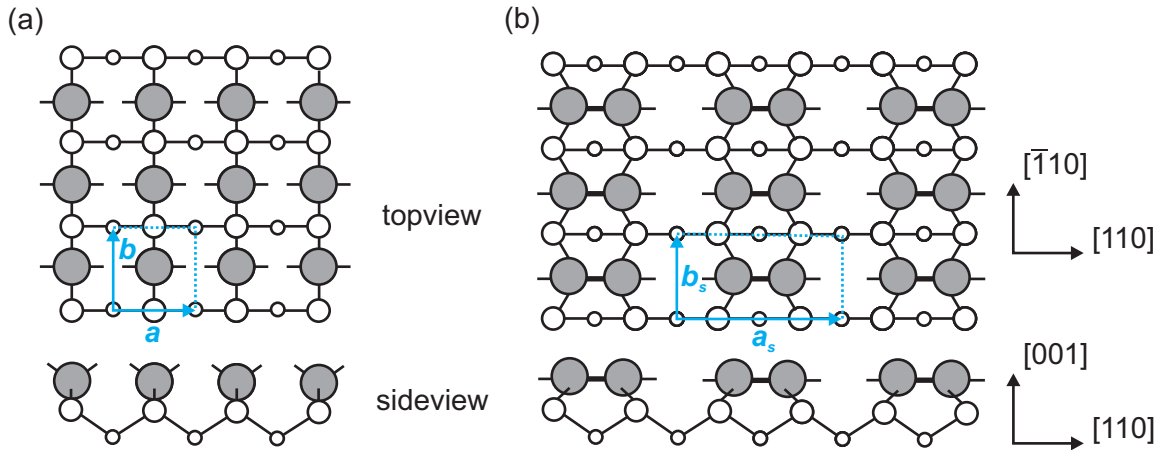
Figure 2.3: (a) Ideal bulk terminated Si(100) surface. (b) Reconstructed Si(100)(2 × 1) surface. The unsaturated bonds of the topmost atoms (gray) favor the formation of dimer rows resulting in a larger unit cell given by $\boldsymbol{a_s}$ and $\boldsymbol{b_s}$. Image taken and adapted from Ref. [33].

At the surface the physical and chemical properties can differ from the bulk structure. For instance, it is possible that a bulk structure does not exhibit the lowest surface energy due to unsaturated bonds. As a consequence relaxation effects and surface reconstructions can appear. If the surface structure differs from the bulk, a second unit cell with the translation operation

$$\boldsymbol{T_s} = u\boldsymbol{a_s} + v\boldsymbol{b_s} \quad \text{with} \quad u, v \in \mathbb{Z} \tag{2.3}$$

is necessary to describe the surface lattice. In general the relationship between the surface and bulk lattice can be expressed in the matrix notation developed by Park and Madden [36] with

$$\begin{pmatrix} \boldsymbol{a_s} \\ \boldsymbol{b_s} \end{pmatrix} = \begin{pmatrix} m_{11} & m_{12} \\ m_{21} & m_{22} \end{pmatrix} \begin{pmatrix} \boldsymbol{a} \\ \boldsymbol{b} \end{pmatrix} \quad \text{with} \quad m_{ij} \in \mathbb{Z}. \tag{2.4}$$

If the two lattices are commensurable ($\angle(\boldsymbol{a}, \boldsymbol{b}) = \angle(\boldsymbol{a_s}, \boldsymbol{b_s})$) the more convenient Wood notation [37]

$$X \, (hkl) \left(\frac{a_s}{a} \times \frac{b_s}{b} \right) \mathrm{R}\alpha \tag{2.5}$$

5

can be applied. Here, (hkl) denotes the surface plane of the bulk material X and Rα describes the rotation angle between the two lattices.

For example, Si(100) exhibits a surface reconstruction as shown in Fig. 2.3. The superstructure is denoted as

$$
\begin{pmatrix} \boldsymbol{a_s} \\ \boldsymbol{b_s} \end{pmatrix} = \begin{pmatrix} 2 & 0 \\ 0 & 1 \end{pmatrix} \begin{pmatrix} \boldsymbol{a} \\ \boldsymbol{b} \end{pmatrix}
\tag{2.6}
$$

in the matrix notation and as

$$
\text{Si}(100)(2 \times 1)
\tag{2.7}
$$

in the Wood notation.

2.1.4 Lattice mismatch and strain effects

In this work films epitaxially grown on crystalline substrates are investigated. Epitaxial means that the films are single crystalline and exhibit a specific crystallographic orientation with respect to the substrates. Often the lattice parameter of the films differ from the substrate parameter which is quantified as lattice mismatch

$$
\epsilon = \frac{a_{\text{film}} - a_{\text{sub}}}{a_{\text{sub}}} .
\tag{2.8}
$$

Here, a_{sub} and a_{film} denote the lateral lattice parameter of the substrate and the film, respectively. The lattice mismatch induces stress which results either in the formation of misfit dislocation or pseudomorphic growth dependent on the free energy density [33]. Misfit dislocation are formed at the interface between film and substrate if the lattice mismatch is relatively large.

Pseudomorphic growth is favored for systems exhibiting a small lattice mismatch. Here, the film is strained so that the lateral lattice constants of the film are expanded or compressed to match the lateral lattice constants of the substrate (cf. Fig. 2.4). As a consequence the vertical lattice constant is expanded for in-plane compression and compressed for in-plane expansion. The energy needed to strain the film increases with the film thickness. Hence, after a critical thickness is reached misfit dislocations are energetically favored resulting a transition from pseudomorphic growth to dislocation formation.

In this work cubic films with (111) orientation are investigated. By assuming a tetragonally distorted film with biaxial in-plane strain, Hashimoto et al. [38] have derived the expression

$$
\frac{\Delta a}{a_{\text{bulk}}} = -\frac{1 - \nu}{2\nu} \frac{\Delta c}{c_{\text{bulk}}} ,
\tag{2.9}
$$

describing the relationship between vertical and lateral strain. Here, Δa and Δc denote the deviation from the unstrained lateral and vertical lattice constant a_{bulk} and c_{bulk}, respectively. The Poisson ratio ν is a material specific constant which can be calculated from the elastic constants [39, 40].
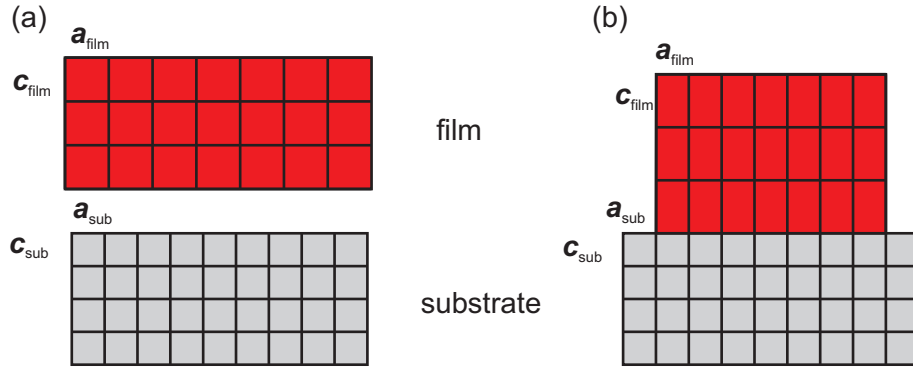
Figure 2.4: Sketch of a pseudomorhic growth. (a) Stand alone film independent of substrate influence. The vertical and lateral lattice constants a_{film} and c_{film} are larger than the corresponding substrate constants a_{sub} and c_{sub}. (b) Pseudomorphic growth of the film results in a compression of the lateral lattice constant a_{film}. The induced tensile strain leads to an expansion of the vertical lattice constant c_{film}.

2.2 X-ray diffraction

The phenomenon of x-ray diffraction can be used to determine the structure of crystalline solids. If matter is irradiated by x-rays, mainly the electrons localized at the atoms act as scattering centers of the incident waves. Constructive and destructive interference can be observed if the atoms are ordered periodically.

The appearance of diffraction maxima, so called Bragg peaks, can be described by Bragg's law [41]

$$2d \sin(\theta) = n\lambda \quad \text{with} \quad n \in \mathbb{Z}. \tag{2.10}$$

Here, d denotes the layer spacing, θ the incident angle and λ the wavelength of the x-rays. The incident waves defined by the wave vector $\boldsymbol{k}_{\text{inc}}$ are reflected at parallel lattice planes resulting in a path difference g of the reflected waves (cf. Fig. 2.5). Constructive interference is observed when this path difference is equal to an integer multiple of the wavelength λ. The value n is called diffraction order. Due to Bragg's law the wavelength of the incident wave must be of the same order as the atomic distances of the probed structure.

An alternative formulation of Bragg's law is given by the Laue equations [42]

$$\boldsymbol{K} \cdot \boldsymbol{a} = 2\pi h, \tag{2.11}$$
$$\boldsymbol{K} \cdot \boldsymbol{b} = 2\pi k, \tag{2.12}$$
$$\boldsymbol{K} \cdot \boldsymbol{c} = 2\pi l. \tag{2.13}$$

Here, $\boldsymbol{K} = \boldsymbol{k}_{\text{ref}} - \boldsymbol{k}_{\text{inc}}$ denotes the scattering vector and the vectors $\boldsymbol{a}$, $\boldsymbol{b}$, and $\boldsymbol{c}$ are the translation vectors of the crystal lattice. The Miller indices h, k and l correspond to the different lattice planes (cf. Sec. 2.1). Diffracted intensity is only observed if the Laue conditions are fulfilled. Any other orientation of the scattering vector $\boldsymbol{K}$ leads to zero intensity.
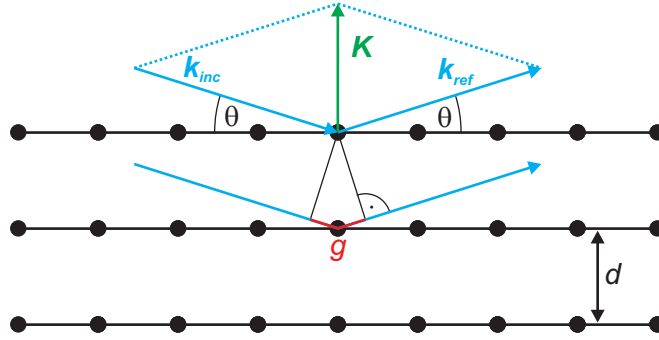
Figure 2.5: Sketch of Bragg's law. The incoming and diffracted waves are defined by the wave vectors $\boldsymbol{k}_{\text{inc}}$ and $\boldsymbol{k}_{\text{ref}}$, respectively. The lattice planes exhibit a layer distance d. The waves reflected at deeper planes exhibit a path difference g. If the condition $g = n\lambda$ is fulfilled constructive interference can be observed. The scattering vector $\boldsymbol{K}$ is defined by the difference $\boldsymbol{k}_{\text{ref}} - \boldsymbol{k}_{\text{inc}}$.

Diffraction phenomena are usually described in the reciprocal space. The basis of the reciprocal space is given by the reciprocal lattice vectors $\boldsymbol{a^*}$, $\boldsymbol{b^*}$ and $\boldsymbol{c^*}$. These vectors are directly related to the real space translation vectors and given by

$$\boldsymbol{a^*} = 2\pi \frac{\boldsymbol{b} \times \boldsymbol{c}}{\boldsymbol{a} \cdot (\boldsymbol{b} \times \boldsymbol{c})}, \tag{2.14}$$

$$\boldsymbol{b^*} = 2\pi \frac{\boldsymbol{c} \times \boldsymbol{a}}{\boldsymbol{a} \cdot (\boldsymbol{b} \times \boldsymbol{c})}, \tag{2.15}$$

$$\boldsymbol{c^*} = 2\pi \frac{\boldsymbol{a} \times \boldsymbol{b}}{\boldsymbol{a} \cdot (\boldsymbol{b} \times \boldsymbol{c})}. \tag{2.16}$$

The scattering vector $\boldsymbol{K}$ can be expressed in the basis of the reciprocal space with

$$\boldsymbol{K} = X\boldsymbol{a^*} + Y\boldsymbol{b^*} + Z\boldsymbol{c^*}. \tag{2.17}$$

The integer values of X, Y and Z correspond to the Miller indices h, k and l. At these positions in reciprocal space the Laue conditions are fulfilled automatically. This makes the concept of reciprocal space very convenient since the reciprocal lattice vectors describe the periodicity of the Bragg peaks in the same manner as the lattice vectors describe the periodicity of the unit cell.

Note that Bragg's law as well as the Laue conditions only give information about the periodicity of the crystal lattice. The structure of the unit cell can additionally influence the diffracted intensity of the Bragg peaks. A Bragg peak is called structural forbidden peak if the intensity is zero due to destructive interference from atoms within one unit cell.

No quantitative analysis is possible by the theory described so far. Therefore, in the following we derive expressions for the diffracted intensities of semi-infinite and thin film structures. This derivation is based on the theoretical work found in Refs. [43–46]. The scattering of x-rays in solids can be described by means of kinematic diffraction theory. Multiple scattering

effects can be neglected due to the small interactions of x-rays with matter. Furthermore, scattered intensity from the nuclei must not be considered based on their small cross sections with x-rays. Thus, the diffracted intensity is determined by the electron density and can be modeled by a summation of all contributions due to the electrons.

2.2.1 Scattering at single electrons

The far field approximation can be made if the distance between radiation source, scattering center and observer are large in comparison with the used wavelength. Since this is the case for x-ray diffraction the incoming and scattered waves can be treated as planar waves. Neglecting inelastically scattered x-rays, the amplitude $A(\boldsymbol{K})$ of a wave scattered at an electron at the position $\boldsymbol{r_e}$ can be described by the Thompson equation

$$A(\boldsymbol{K}) = A_0 C \, e^{\, i \, \boldsymbol{K} \cdot \boldsymbol{r_e}} \quad \text{with} \quad C = \frac{e^2 P^{\frac{1}{2}}}{m_e c^2 R_0} \,. \tag{2.18}$$

Here, A_0 denotes the amplitude of the incident wave, m_e the electron mass, e the charge of the electron, c the speed of light and R_0 the distance between the electron and the observer. The polarization factor P takes into account the polarization of the incidence plane with respect to the scattering plane defined by $\boldsymbol{K}$. Since the polarization of the incidence wave is not changed during the measurements, the polarization factor can be considered constant.

2.2.2 Scattering at single atoms

Scattering at a single atom can be described by summation of the contributions of all its electrons using the Thompson equation (cf. Eq. 2.18). The phase differences of the scattered waves have to be considered due to the different positions $\boldsymbol{r}$ of the electrons within the atom. Furthermore, the electrons are not localized at distinct positions. The delocalization is taken into account by an electron density distribution $\rho(\boldsymbol{r})$. The amplitude of a scattered wave is given by

$$\begin{aligned} A(\boldsymbol{K}) &= A_0 C \int d^3 r \, \rho(\boldsymbol{r}) \, e^{\, i \, \boldsymbol{K} \cdot (\boldsymbol{r_a} + \boldsymbol{r})} \tag{2.19} \\ &= A_0 C \, f(\boldsymbol{K}) \, e^{\, i \, \boldsymbol{K} \cdot \boldsymbol{r_a}} \,, \tag{2.20} \end{aligned}$$

with $\boldsymbol{r_a}$ as the position of the atom. Furthermore, the integration of the electron density is defined as atomic form factor

$$f(\boldsymbol{K}) = \int d^3 r \, \rho(\boldsymbol{r}) \, e^{\, i \, \boldsymbol{K} \cdot \boldsymbol{r}} \,, \tag{2.21}$$

which corresponds to the Fourier transformation of the electron density. Assuming a spherical electron distribution, the form factor only depends on the absolute value K of the scattering vector. It can be approximated by four Gaussian functions

$$f(K) = \sum_{i=1}^{4} a_i \, e^{-b_i \left(\frac{K}{4\pi} \right)^2} + c \,. \tag{2.22}$$

Tabulated values for a_i, b_i and c can be found in Ref. [47].

2.2.3 Scattering at single unit cells

The amplitude of scattered x-rays at a unit cell can be calculated by summation of the scattering amplitude of all atoms inside the unit cell. Here, analogous to the single atom the phase differences of the scattered waves have to be taken into account. The amplitude is given by

$$A(\boldsymbol{K}) = A_0 C \sum_{j=1}^{N} f_j(K) \, e^{i\,\boldsymbol{K}\cdot(\boldsymbol{r_n}+\boldsymbol{r_j})} \tag{2.23}$$

$$= A_0 C \, F(\boldsymbol{K}) \, e^{i\,\boldsymbol{K}\cdot\boldsymbol{r_n}}\,, \tag{2.24}$$

with N as the number of atoms in the unit cell. The position of the unit cell is given by $\boldsymbol{r_n}$ while the positions of the atoms within the unit cell are given by $\boldsymbol{r_j}$. Similar to the atomic form factor, the structure factor is defined by

$$F(\boldsymbol{K}) = \sum_{j=1}^{N} f_j(K) \, e^{i\,\boldsymbol{K}\cdot\boldsymbol{r_j}}\,, \tag{2.25}$$

which is the Fourier transformation of the electron density distribution of the unit cell. In contrast to the atomic form factor, the structure factor is a function of the vector $\boldsymbol{K}$.

Thermal vibrations can lead to deviations of the atoms from their ideal positions. The deviations can be modeled by a Gaussian distribution [48] and results in a modified average structure factor

$$\overline{F}(D,\boldsymbol{K}) = e^{-DK^2} \sum_{j=1}^{N} f_j(K) \, e^{i\,\boldsymbol{K}\cdot\boldsymbol{r_j}}\,. \tag{2.26}$$

Here D denotes the Debye Waller factor describing the thermal vibrations. The scattered intensity is damped by increasing absolute value of the scattering vector $\boldsymbol{K}$. Detailed derivations addressing the thermal influence can be found in Refs. [49,50].

2.2.4 Diffraction at single crystals

A single crystal is formed by an infinite repetition of a unit cell according to its crystal lattice (cf. Eq. 2.1). Due to this periodic arrangement diffraction phenomena can be observed. The diffraction amplitude can be calculated by the summation of the diffraction amplitudes of all unit cells under consideration of the phase shifts via

$$A(\boldsymbol{K}) = A_0 C \sum_{n} F_n(\boldsymbol{K}) \, e^{i\,\boldsymbol{K}\cdot\boldsymbol{r_n}}\,. \tag{2.27}$$

The periodicity of the unit cells can be described by the translation vectors $\boldsymbol{a}$, $\boldsymbol{b}$ and $\boldsymbol{c}$ (cf. Sec. 2.1.1). Assuming an identical form factor $F(\boldsymbol{K})$ for each unit cell, Eq. (2.27) can be rewritten to

$$
\begin{aligned}
A(\boldsymbol{K}) &= A_0 C\, F(\boldsymbol{K}) \sum_{n_1=0}^{N_1-1} \sum_{n_2=0}^{N_2-1} \sum_{n_3=0}^{N_3-1} e^{\,i\boldsymbol{K}\,\cdot\,(n_1\boldsymbol{a}+n_2\boldsymbol{b}+n_3\boldsymbol{c})} \qquad (2.28) \\
&= A_0 C\, F(\boldsymbol{K}) \sum_{n_1=0}^{N_1-1} e^{\,i\,n_1\,\boldsymbol{K}\cdot\boldsymbol{a}} \sum_{n_2=0}^{N_2-1} e^{\,i\,n_2\,\boldsymbol{K}\cdot\boldsymbol{b}} \sum_{n_3=0}^{N_3-1} e^{\,i\,n_3\,\boldsymbol{K}\cdot\boldsymbol{c}} . \qquad (2.29)
\end{aligned}
$$

Here, the translation vectors and the number of unit cells in each spatial direction are given by $\boldsymbol{a}$, $\boldsymbol{b}$ and $\boldsymbol{c}$ and N_1, N_2 and N_3, respectively. The summation of the unit cells in one
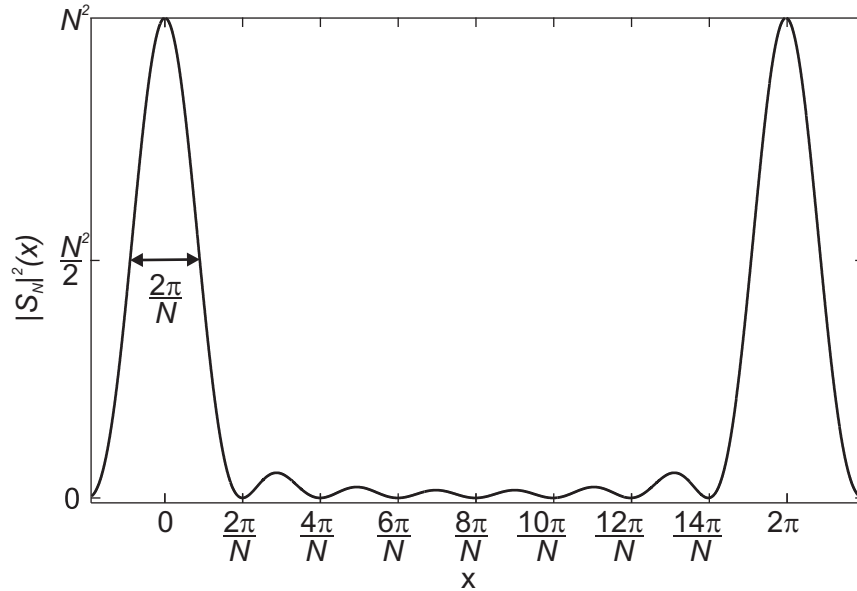

Figure 2.6: N-slit function for $N = 8$. The main maxima are separated by a multiple of 2π and $N - 2$ fringes are visible. The full width at half maximum (FWHM) of the main peaks and distance between the fringes are given by $2\pi/N$.

direction is equal to the geometric series, for instance

$$
S_N(\boldsymbol{K}) = \sum_{n=0}^{N-1} e^{\,i\,n\,\boldsymbol{K}\cdot\boldsymbol{c}} = \frac{1 - e^{\,i\,N\,\boldsymbol{K}\cdot\boldsymbol{c}}}{1 - e^{\,i\,\boldsymbol{K}\cdot\boldsymbol{c}}} . \qquad (2.30)
$$

By substituting $x = \boldsymbol{K}\cdot\boldsymbol{c}$ the diffracted intensity of a one dimensional structure can be calculated by squaring of Eq. (2.30) resulting in

$$
|S_N|^2(x) = \frac{\sin^2(N\,x/2)}{\sin^2(x/2)} . \qquad (2.31)
$$

11

This equation is known as N-slit function (cf. Fig. 2.6) which is commonly used to describe diffraction for one dimensional gratings. The N-slit function exhibits N maxima separated by a multiple of 2π. Furthermore, $N-2$ fringes can be observed between the main maxima. The width of the maxima and the fringes scale with the number of slits. The width of the features decreases with increasing number of slits. For an ideal single crystal with infinite spatial expansion ($N \to \infty$) the fringes vanish and the maxima become δ-peaks with infinite intensity.

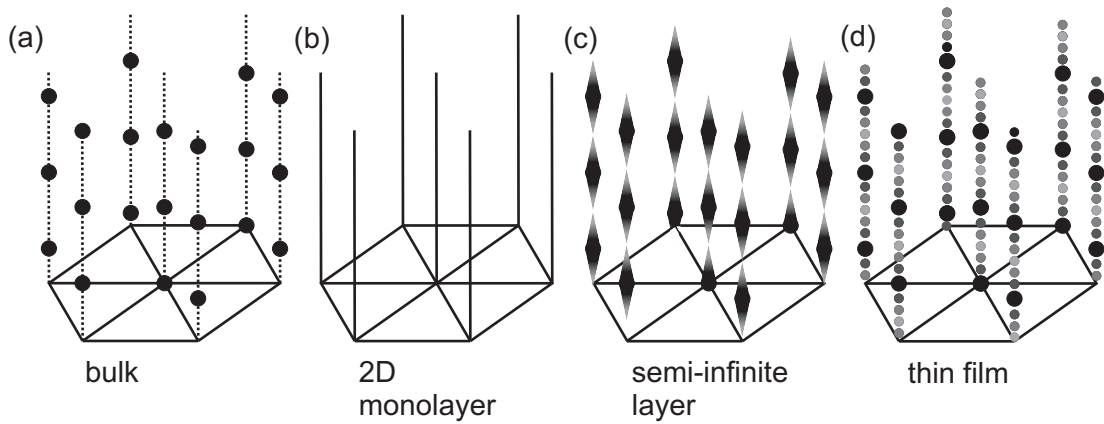### 2.2.5 Diffraction at semi-infinite crystals

Figure 2.7: Sketch of the reciprocal space for a infinite bulk crystal (a), a 2D layer (b), a semi-infinte crystal (c) and a thin film (d). The diffracted intensity of an infinite crystal is described by sharp Bragg peaks with infinite intensity. Due to the reduced translation symmetry the 2D layer shows no distinct Bragg peaks but diffraction rods. For a semi-infinite crystal the Bragg peaks are smeared out resulting in crystal truncation rods (CTRs). Thin films show defined oscillations between the Bragg peaks based on their finite size.

The concept of a semi-infinite crystal is used to model the diffracted intensity of the substrates used in this thesis. Here, the translation symmetry given for an infinite crystal is limited in vertical direction. In addition, absorption effects limiting the penetration depth of the x-rays have to be taken into account. These effects result in so called crystal truncation rods (CTRs) as depicted in Fig. 2.7 (c).

If absorption is neglected, an infinite crystal exhibits sharp Bragg peaks with infinite intensity as depicted in Fig. 2.7 (a). In contrast, for a two dimensional plane ($N_3 = 1$), the intensity contributions of the out-of-plane direction becomes constant resulting in rods of homogeneous intensity (cf. Fig. 2.7 (b)). The lateral position of these rods are still defined by the two dimensional infinite surface lattice.

Taking into account the penetration depth of x-rays in semi-infinite crystals, only a limited number of layers contribute to the intensity. Deeper layers of the crystal have a smaller

contribution compared to the diffracted intensity than the topmost layer due to absorption effects. These effects result in smeared out Bragg peaks as shown in Fig. 2.7 (c).

Considering the absorption of the x-rays the total diffracted amplitude is determined by

$$A(\boldsymbol{K}) = A_0 C\, F(\boldsymbol{K}) \sum_{n_1=0}^{N_1-1} e^{i\, n_1\, \boldsymbol{K}\cdot\boldsymbol{a}} \sum_{n_2=0}^{N_2-1} e^{i\, n_2\, \boldsymbol{K}\cdot\boldsymbol{b}} \sum_{n_3=-\infty}^{N_3(n_1,n_2)} e^{i\, n_3\, \boldsymbol{K}\cdot\boldsymbol{c}\, +\, n_3\epsilon}\,.$$

(2.32)

Here, ϵ denotes the absorption from one layer to the next one. The roughness of the surface given by the lateral height variation is described by the function $N_3(n_1, n_2)$ (cf. Fig. 2.8). Assuming an infinite expansion in the lateral directions, the intensity can be determined using
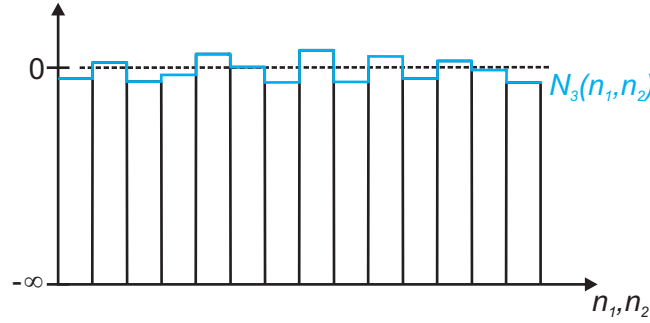

Figure 2.8: Schematic drawing of a semi-infinite crystal. The step height at an individual point (n_1, n_2) in the lateral plane is described by the function N_3 while the average value is at zero level.

Eq. (2.32) and is given by

$$A(\boldsymbol{K}) = A_0 C\, F(\boldsymbol{K}) \sum_{n_1=0}^{N_1-1} 1 \sum_{n_2=0}^{N_2-1} 1 \sum_{n_3=-\infty}^{N_3(n_1,n_2)} e^{i\, n_3\, \boldsymbol{K}\cdot\boldsymbol{c}\, +\, n_3\epsilon}$$

(2.33)

$$= A_0 C\, F(\boldsymbol{K}) \sum_{n_1=0}^{N_1-1} \sum_{n_2=0}^{N_2-1} \frac{e^{(i\, \boldsymbol{K}\cdot\boldsymbol{c}\, +\, \epsilon)N_3(n_1,n_2)}}{1 - e^{-(i\, \boldsymbol{K}\cdot\boldsymbol{c}\, +\, \epsilon)}}\,.$$

(2.34)

The sums over n_1 and n_2 correspond to an averaging over the height function $N_3(n_1, n_2)$ with an average value at zero level resulting in

$$A(\boldsymbol{K}) = A_0 C\, F(\boldsymbol{K})\, N_1 N_2 \frac{\left\langle e^{(i\, \boldsymbol{K}\cdot\boldsymbol{c}\, +\, \epsilon)N_3(n_1,n_2)} \right\rangle}{1 - e^{-(i\, \boldsymbol{K}\cdot\boldsymbol{c}\, +\, \epsilon)}}\,.$$

(2.35)

The average of the function can be approximated by a Gaussian distribution as described in Ref. [46]. Thus, the diffracted amplitude can be written as

$$A(\boldsymbol{K}) = A_0 C\, F(\boldsymbol{K})\, N_1 N_2 \frac{e^{-\sigma^2(1 - \cos(\boldsymbol{K}\cdot\boldsymbol{c}))}}{1 - e^{-(i\, \boldsymbol{K}\cdot\boldsymbol{c}\, +\, \epsilon)}}\,,$$

(2.36)

with σ as the root mean square roughness of the surface of the semi-infinite crystal.
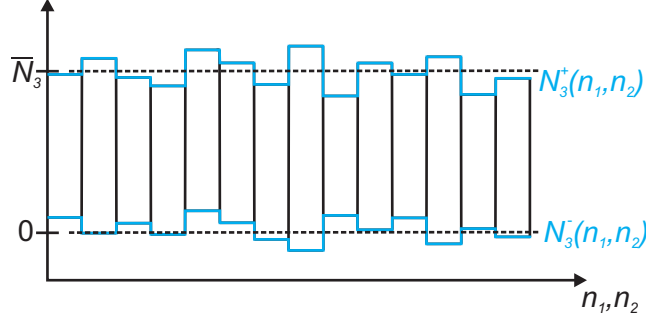
2.2.6 Diffraction at thin films

Figure 2.9: Schematic drawing of a thin film with the average film thickness of $\overline{N}_3$. The roughness of the bottom and top side is given by $N_3^-(n_1, n_2)$ and $N_3^+(n_1, n_2)$, respectively.

The diffracted amplitude of a thin film can be modeled quite similar to a semi-infinite crystal. A few modifications have to be considered. First, the damping ϵ described above can be neglected due to the small finite size of the film in comparison with the penetration depth of the x-rays. Second, the roughness at both interfaces at the top and the bottom of the film has to be taken into account. This is done by two height function $N_3^+(n_1, n_2)$ and $N_3^-(n_1, n_2)$ for the top and bottom side, respectively (cf. Fig. 2.9). The average height value at the bottom and top side are zero and $\overline{N}_3$, respectively. Thus, the diffracted amplitude is given by

$$A(\boldsymbol{K}) = A_0 C \, F(\boldsymbol{K}) \sum_{n_1=0}^{N_1-1} 1 \sum_{n_2=0}^{N_2-1} 1 \sum_{n_3=N_3^-(n_1,n_2)}^{N_3^+(n_1,n_2)} e^{i\, n_3\, \boldsymbol{K}\cdot\boldsymbol{c}} \tag{2.37}$$

$$= A_0 C \, F(\boldsymbol{K}) \sum_{n_1=0}^{N_1-1} \sum_{n_2=0}^{N_2-1} \frac{e^{i\,\boldsymbol{K}\cdot\boldsymbol{c}\, N_3^-(n_1,n_2)} - e^{i\,\boldsymbol{K}\cdot\boldsymbol{c}\, N_3^+(n_1,n_2)+1}}{1 - e^{i\,\boldsymbol{K}\cdot\boldsymbol{c}}} \, . \tag{2.38}$$

Similar to the semi-infinite crystal, the sums can be treated as averaging which results in

$$A(\boldsymbol{K}) = A_0 C \, F(\boldsymbol{K}) \, N_1 N_2 \frac{\left\langle e^{i\,\boldsymbol{K}\cdot\boldsymbol{c} u_c^-} \right\rangle - e^{i\,\boldsymbol{K}\cdot\boldsymbol{c}\overline{N}_3} \left\langle e^{i\,\boldsymbol{K}\cdot\boldsymbol{c} u_c^+} \cdot \right\rangle}{1 - e^{i\,\boldsymbol{K}\cdot\boldsymbol{c}}} \tag{2.39}$$

Here u_c^+ and u_c^- denote the deviation from the average film thickness N_3 at the top and bottom side, respectively. By assuming Gaussian distributions for the deviations, the equation can be approximated by

$$A(\boldsymbol{K}) = A_0 C \, F(\boldsymbol{K}) \, N_1 N_2 \frac{e^{-\sigma_-^2(1-\cos(\boldsymbol{K}\cdot\boldsymbol{c}))} - e^{i\,\boldsymbol{K}\cdot\boldsymbol{c}\overline{N}_3} e^{-\sigma_+^2(1-\cos(\boldsymbol{K}\cdot\boldsymbol{c}))}}{1 - e^{i\,\boldsymbol{K}\cdot\boldsymbol{c}}} \, . \tag{2.40}$$

The intensity distribution of a thin film is shown in Fig. 2.7 (d).

2.2.7 Diffraction at a thin film systems

The multilayer system investigated in this thesis are considered to grow pseudomorphically. This means the positions of the CTRs of the substrate and the film coincide. Therefore, the diffracted amplitude for the CTRs of such a system can be calculated by summation of all contributions under consideration of the phase relationships between the layers:

$$A\left(\boldsymbol{K}\right) = A_{\text{substrate}}\left(\boldsymbol{K}\right) + \sum_{m=1}^{M} \Theta_m\, e^{i\boldsymbol{K}\cdot\boldsymbol{p}_m}\, A_{\text{film},m}\left(\boldsymbol{K}\right). \tag{2.41}$$

Here, M denotes the number of layers and Θ_m denotes the fill factor of each individual layer. The fill factor takes into account impurities and dislocation in the film reducing the intensity contribution. The phase vector $\boldsymbol{p}_m$ is defined by

$$\boldsymbol{p}_m = \sum_{j=1}^{m-1} \boldsymbol{g}_j + \overline{N}_{3,j}\boldsymbol{c}_j\,, \tag{2.42}$$

where $\boldsymbol{g}_j$ denotes the interface vector defining the distance between the layers j and $j+1$. The phase shift given by the film thickness of layer j is denoted $\overline{N}_{3,j}\boldsymbol{c}_j$. Thus, the term $e^{i\boldsymbol{K}\cdot\boldsymbol{p}_m}$ describes the phase relationship between the layers.

2.3 Low energy electron diffraction

Low energy electron diffraction (LEED) is used to probe the structure and morphology of crystalline surfaces. Electrons exhibit a de Broglie wavelength of the same order as the inter-atomic distances, thus, diffraction phenomena can be observed. The de Broglie wavelength is given by

$$\lambda_e = \frac{2\pi\hbar}{\sqrt{2m_e E}}\,. \tag{2.43}$$

Here, $\hbar$ denotes the reduced Plank constant, m_e the electron mass and E the kinetic energy of the electrons. The probing depth of LEED is limited to the near-surface region due to the strong interaction of electrons with matter. Typically electron energies in the range of 10 - 500 eV are used in LEED experiments resulting in a mean free path of $\approx$ 10 Å (cf. Fig. 2.10). In contrast to x-ray diffraction multiple scattering effects have to be taken into account due to the strong interaction of electrons with matter. Therefore, a full analysis of electron diffraction pattern is only possible within dynamic diffraction theory [52]. The dynamic calculations become very complex if defects are present at the surface. However, a determination of the surface morphology becomes more easy if the analysis is limited to the spot profile.
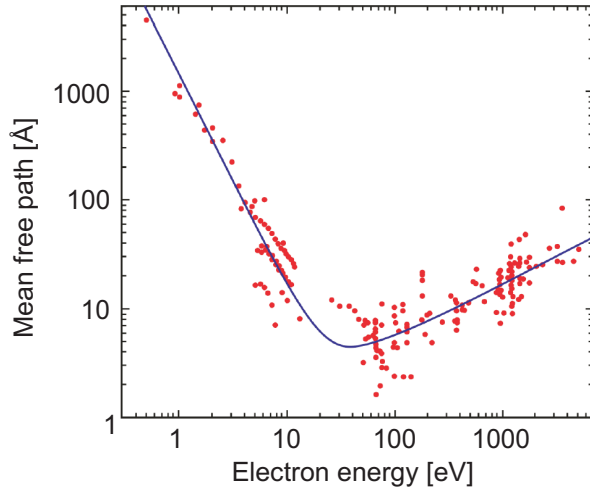
Figure 2.10: Inelastic mean free path of an electron against kinetic energy. Image taken and adapted form Ref. [51].

The behavior of the spot profile can be modeled by a modified kinematic diffraction theory as presented in the following. In contrast to the XRD theory (cf. Sec. 2.2.3) the unit cells are defined as columns as depicted in Fig. 2.11. This is necessary to consider the multiple scattering processes. Electrons are mainly scattered in forward direction. Therefore, scattering within the atomic layers can be neglected if the incident angle is close to the surface normal. Thus, the column shaped unit cells can be used to approximate the multiple scattering processes.
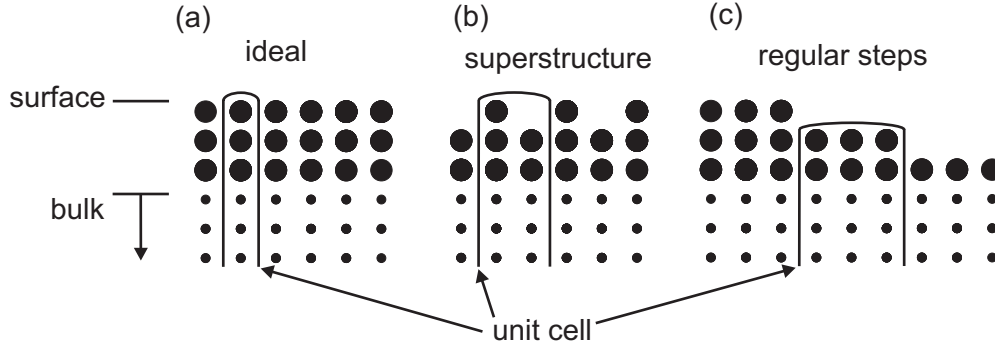

Figure 2.11: Examples of unit cells used in kinematic LEED theory. Image taken and adapted from Ref. [53].

2.3.1 Electron diffraction at an ideal surface

The amplitude of a diffracted electron wave at a surface with infinite lateral expansion is given by

$$A(\boldsymbol{K}) = \frac{1}{\sqrt{\mathcal{N}}} \sum_{n=-\infty}^{\infty} f_n(\boldsymbol{K})\, e^{i\boldsymbol{K} \cdot \boldsymbol{r}_n} \ . \tag{2.44}$$

16

Here, the positions of the unit cells are given by $\boldsymbol{r}_n$ and $\mathcal{N}$ denotes the normalization constant. The factor $f_n(\boldsymbol{K})$ represents the scattering amplitude of the nth column shaped unit cell. Appearing multiple scattering processes are approximated within this factor. The total diffracted intensity is given by the square of the amplitude

$$I(\boldsymbol{K}) = |A(\boldsymbol{K})|^2 = \frac{1}{\mathcal{N}} \sum_{n=-\infty}^{\infty} \sum_{m=-\infty}^{\infty} f_n(\boldsymbol{K}) f_m^*(\boldsymbol{K}) \, e^{\, i\boldsymbol{K} \cdot (\boldsymbol{r}_n - \boldsymbol{r}_m)} \, . \tag{2.45}$$

Assuming a similar scattering behavior for each column ($f(\boldsymbol{K}) = f_n(\boldsymbol{K})$) the intensity can be split into two contributions following

$$I(\boldsymbol{K}) = \frac{1}{\mathcal{N}} \, F(\boldsymbol{K}) \, G(\boldsymbol{K}). \tag{2.46}$$

Here, $F(\boldsymbol{K}) = |f(\boldsymbol{K})|^2$ denotes the dynamical form factor which considers the scattering within the columns. The contribution of the ordering of the columns

$$G(\boldsymbol{K}) = \sum_{n=-\infty}^{\infty} \sum_{m=-\infty}^{\infty} e^{\, i\boldsymbol{K} \cdot (\boldsymbol{r}_n - \boldsymbol{r}_m)} \tag{2.47}$$

is called lattice factor and defines the shape of the diffraction spots and their positions. According to Ref. [54] the normalization constant $\mathcal{N}$ has to be chosen that integration over the first Brillouin zone (BZ) fulfills the condition

$$\int_{\mathrm{BZ}} d\boldsymbol{K}_{\parallel} G(\boldsymbol{K}) = 1. \tag{2.48}$$

An ideal surface consists of columns located at lattice points ($\boldsymbol{r}_n = n_1 \boldsymbol{a} + n_2 \boldsymbol{b}$) and exhibits no height variations. Thus, the lattice factor is independent of the vertical component $\boldsymbol{K}_{\perp}$ of the scattering vector and consist of δ-functions located at the corresponding lateral positions in reciprocal space:

$$G_{\mathrm{ideal}}(\boldsymbol{K}) = \sum_{n=-\infty}^{\infty} \delta(\boldsymbol{K}_{\parallel} - (m_1 \boldsymbol{a}^* + m_2 \boldsymbol{b}^*)) \quad \text{with} \quad m_1, m_2 \in \mathbb{Z} \, . \tag{2.49}$$

This leads to the diffraction rods depicted in Fig. 2.7 (b).

2.3.2 Spot profile analysis of surfaces with randomly distributed steps

Deviations from the ideal surface, i. e. steps or inhomogeneities, have a strong impact on the spot profile [55–57]. Usually $F(\boldsymbol{K})$ shows only weak dependence of the parallel component $\boldsymbol{K}_{\parallel}$ of the scattering vector [52]. Thus, only the dominating lattice factor $G(\boldsymbol{K})$ has to be considered in spot profile analysis.

In the following a method is presented to analyze rough surfaces with atomic step heights based on the derivations made in Refs. [58–60]. For reasons of simplicity we start with the discussion of the one dimensional case. Only steps of single height or multiple of the atomic
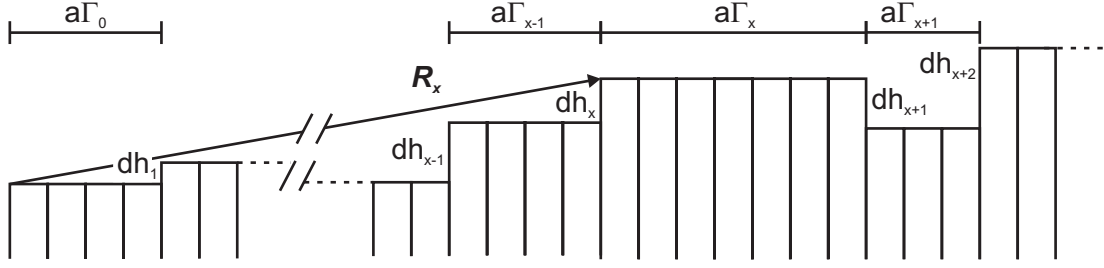
Figure 2.12: One dimensional sketch of random distributed terraces with random atomic step heights. The terrace width is a multiple Γ of the lateral lattice constant a while the step height is multiple h of the single atomic step height d. The position of the nth terrace is defined by the vector $\boldsymbol{R}_n$.

step height d are considered. It is assumed that atoms from different layers lie on top of each other. In addition, the steps are displaced only in the direction perpendicular to the surface. Other vertical and lateral displacements are not taken into account.

Fig. 2.12 shows a sketch of a surface with random distributed terraces with random atomic step heights. Adjacent columns of the same height can be combined to terraces of the width $a\Gamma_x$. These terraces are considered as domains with similar scattering behavior. The corresponding lattice factor can be written as

$$G(\boldsymbol{K}) = \sum_{x=-\infty}^{\infty} \sum_{y=-\infty}^{\infty} S_x(\boldsymbol{K}) S_y^*(\boldsymbol{K}) \, e^{i\boldsymbol{K} \cdot (\boldsymbol{R}_x - \boldsymbol{R}_y)} \,. \tag{2.50}$$

Here, the structural amplitude $S_x(\boldsymbol{K})$ of the xth terrace at the position $\boldsymbol{R}_x$ is defined by

$$S_x(\boldsymbol{K}) = \frac{1 - e^{i\boldsymbol{K}_{||}a\Gamma_x}}{1 - e^{i\boldsymbol{K}_{||}a}} \,. \tag{2.51}$$

with a as lateral lattice constant and $a\Gamma_x$ as the width of the xth terrace. Using the unit vectors parallel ($\boldsymbol{e}_{||}$) and perpendicular ($\boldsymbol{e}_{\perp}$) to the surface the position of the xth terrace can be written as

$$\boldsymbol{R}_x = \sum_{j=0}^{x-1} a\Gamma_j \boldsymbol{e}_{||} + \sum_{j=1}^{x} dh_j \boldsymbol{e}_{\perp} \,, \tag{2.52}$$

where dh_j denotes the step height. Therefore, the lattice factor can be written as

$$G(\boldsymbol{K}) = \sum_{x=-\infty}^{\infty} \sum_{y=-\infty}^{\infty} S_x(\boldsymbol{K}) S_y^*(\boldsymbol{K}) \, e^{i\boldsymbol{K}_{||}a\left(\sum_{j=0}^{x-1} \Gamma_j - \sum_{j=0}^{y-1} \Gamma_j\right)} \, e^{i\boldsymbol{K}_{\perp}d\left(\sum_{j=1}^{x} h_j - \sum_{j=1}^{y} h_j\right)} \,. \tag{2.53}$$

By definition the domains are located at multiples of the lattice vectors. Hence, the sums can be re-indexed and simplified to

$$G(\boldsymbol{K}) = \sum_{x=-\infty}^{\infty} \sum_{y=-\infty}^{\infty} S_{x+y}(\boldsymbol{K}) S_y^*(\boldsymbol{K}) \, e^{i\boldsymbol{K}_\| a \sum_{j=y}^{x+y-1} \Gamma_j} \, e^{i\boldsymbol{K}_\perp d \sum_{j=y+1}^{x+y} h_j} \qquad (2.54)$$

$$= \sum_{x=-\infty}^{\infty} \left\langle S_{x+y}(\boldsymbol{K}) S_y^*(\boldsymbol{K}) \, e^{i\boldsymbol{K}_\| a \sum_{j=y}^{x+y-1} \Gamma_j} \, e^{i\boldsymbol{K}_\perp d \sum_{j=y+1}^{x+y} h_j} \right\rangle_y \qquad (2.55)$$

with $\langle ... \rangle_y$ as averaging with respect to y. As shown in Appx. A this equation can be further simplified to

$$G(\boldsymbol{K}) = \frac{1}{2(1 - \cos(\boldsymbol{K}_\| a))} \left(\frac{(1 - \beta_S(\boldsymbol{K}_\perp))(1 - \beta_T(\boldsymbol{K}_\|))}{1 - \beta_S(\boldsymbol{K}_\perp) \beta_T(\boldsymbol{K}_\|)} + c.c. \right) , \qquad (2.56)$$

with $\beta_S(\boldsymbol{K}_\perp)$ and $\beta_T(\boldsymbol{K}_\|)$ as the Fourier transformation of the step height and terrace width distributions, respectively (cf. Eq. (A.1) and Eq. (A.2)).

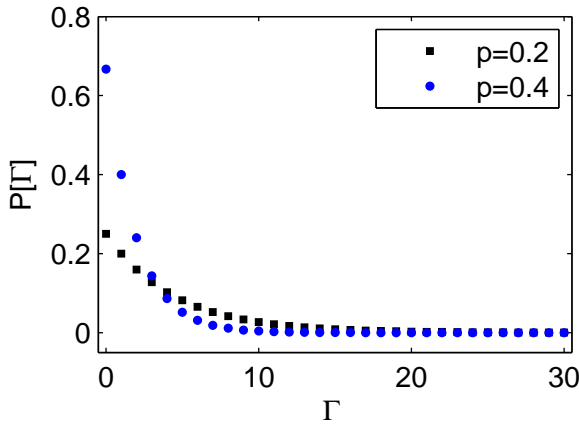**Figure 2.13:** Geometric distribution of terrace widths consisting of Γ unit cells. The probability of finding a step edge by going from one adjacent lattice point to another is denoted by p. Image taken and adapted from Ref. [58].

Assuming the probability for up or down steps is equal, the total probability p of finding a step of any height is given by

$$p = \sum_{i=1}^{I} p_i , \qquad (2.57)$$

where I is the maximal occurring multiple of the atomic step height and p_i the probability for a particular height. Furthermore, by assuming random occurrence of the steps, the terrace width distribution can be described by the geometric distribution

$$P(\Gamma) = (1 - p)^{\Gamma - 1} p . \qquad (2.58)$$

Here, $(1 - p)^{\Gamma - 1}$ denotes the probability of finding no step in the range of $\Gamma - 1$ lattice sites. The probability of finding a step passing from the $\Gamma - 1$ to the Γth lattice site is given by p.

19

The product of these terms now defines the probability of finding a terrace with the width of $a\Gamma$. Examples of the geometric distribution is shown in Fig. 2.13. Smaller terraces are favored before larger terraces. The assumption of a geometric distribution is valid as long as no step-step interactions, e.g. repulsion or coalescence, are present. These interactions would result in larger terraces and are not considered in the following.

In addition to the terrace width distribution a step height distribution must be taken into account. The step height distribution does not directly influence the terrace width distribution but has a strong impact on the profile of the diffraction spots. By assuming uncorrelated step heights, they can also be described with a geometrical distribution. In Ref. [59] it is shown that the intensity contributions of the steps can be approximated by a Lorentzian function

$$G(\boldsymbol{K}) \approx \frac{1}{\kappa^2 + (a\Delta\boldsymbol{K}_{\parallel})^2} \quad \text{with} \quad \kappa = \frac{1 - \beta_S(\boldsymbol{K}_\perp)}{\langle\Gamma\rangle} . \tag{2.59}$$

Here, $\langle\Gamma\rangle$ denotes the average terrace width. For a surface with up and down steps of mono atomic height the FWHM of the Lorentzian function is given by

$$a\Delta\boldsymbol{K}_{\parallel} = \frac{2(1 - \beta_S(\boldsymbol{K}_\perp))}{\langle\Gamma\rangle} = \frac{2(1 - \cos(d\boldsymbol{K}_\perp))}{\langle\Gamma\rangle} . \tag{2.60}$$

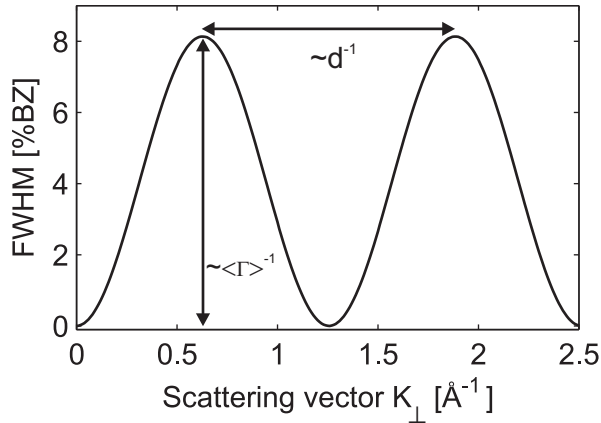Often the experimental data is scaled in percentage of the first Brillouin zone which is defined

Figure 2.14: FWHM of a diffraction rod as a function of $\boldsymbol{K}_\perp$ for a rough surface. The periodicity and amplitude of the oscillations are proportional to the inverse of the step height d and average terrace width $\langle\Gamma\rangle$, respectively.

by the distance of the nearest neighbor reflex positions. Therefore, it is useful to convert the FHWM in units of the first Brillouin zone resulting in

$$\text{FWHM}(\boldsymbol{K}_\perp) = 100\%\text{BZ}\frac{a}{\pi}\left(\frac{1 - \cos(d\boldsymbol{K}_\perp)}{a\langle\Gamma\rangle^*}\right) . \tag{2.61}$$

The vertical component $\boldsymbol{K}_\perp$ of the scattering vector can be calculated directly form the electron energy E with

$$\boldsymbol{K}_\perp = \frac{\cos(\vartheta)\sqrt{2m_e E}}{\hbar} . \tag{2.62}$$

---

*Note, in this section $\langle\Gamma\rangle$ is denoted as number and not in length units as done in Chapter 5 and Chapter 8.

Here, ϑ denotes the angle with respect to the surface normal of the incident electron beam. Thus, the step height and mean terraces width can be determined by an energy dependent analysis of the spot profile. An example for the oscillating FWHM due to mono atomic steps is presented in Fig. 2.14.

Up to now, only the one dimensional case is considered. If the steps are isotropically distributed in the lateral directions, the theory can be easily expanded to two dimension. The Lorentzian function is modified to

$$G(\boldsymbol{K}) \approx \frac{1}{(\kappa^2 + (a\Delta\boldsymbol{K}_{\parallel})^2)^{2/3}} \quad . \tag{2.63}$$

As a consequence Eq. (2.61) expands to

$$\mathrm{FWHM}(\boldsymbol{K}_{\perp}) = 100\%\mathrm{BZ}\sqrt{2^{2/3} - 1}\frac{a}{\pi}\left(\frac{1 - \cos(d\boldsymbol{K}_{\perp})}{a\langle\Gamma\rangle}\right) \quad . \tag{2.64}$$

The prefactor $\sqrt{2^{2/3} - 1}$ considers the isotropic exponentially decaying 2D correlation as shown in Ref. [59].

2.3.3 Mosaics without preferred orientation and grain boundaries

As yet, only random distributed steps are considered for the spot profile analysis. In addition, thin films can exhibit mosaics which are tilted crystalline regions (cf. Fig. 2.15). The different regions are called crystallites or grains. Mosaics can be formed, for instance, in heteroepitactical systems to reduce strain due to large misfit between substrate and film. Individual grains exhibit tilted surface normals and, thus, tilted diffraction rods. If the grains
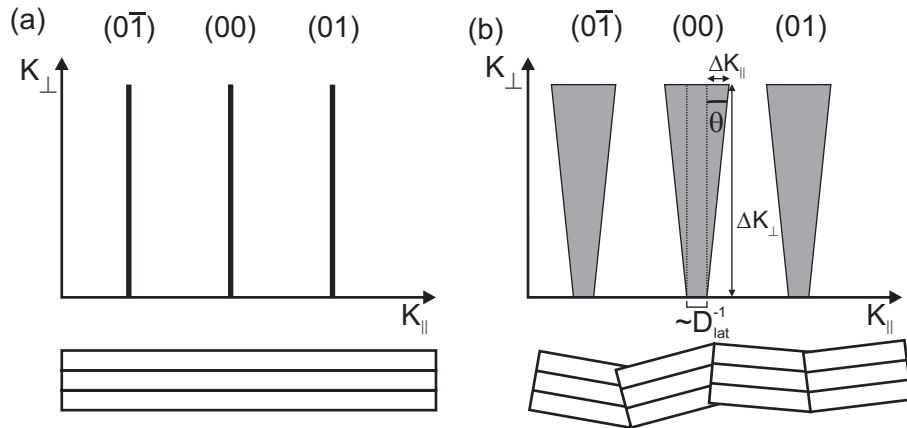

Figure 2.15: (a) Ideal surface: Sharp diffraction rods are visible which are independent of $\boldsymbol{K}_{\perp}$. (b) Surface with mosaics without preferred orientation: The FWHM of the diffraction rods increases for larger values of $\boldsymbol{K}_{\perp}$. The finite grain size D_{lat} results in a constant broadening of the FWHM. The average mosaic angle is given by $\tan(\theta) = \Delta\boldsymbol{K}_{\parallel}/\Delta\boldsymbol{K}_{\perp}$. Image taken and adapted from Ref. [61].

are not oriented in any preferred direction a Gaussian distribution with a standard deviation $\theta \neq 0$ can be assumed [61]. This results in a lateral broadening $\Delta K_{\parallel}$ of the diffraction rods with increasing vertical scattering vector $K_{\perp}$ (cf. Fig. 2.15). The standard deviation θ of the mosaic spread can be determined by

$$\frac{\Delta K_{\parallel}}{\Delta K_{\perp}} = \tan(\theta). \tag{2.65}$$

Furthermore, the Bragg condition is altered at the interface between two grains [62]. The grain boundaries result in an additional constant broadening of the diffraction rods as depicted in Fig. 2.15 (b). Taken these effects into account Eq. (2.64) can be expanded to

$$\text{FWHM}(\boldsymbol{K}_{\perp}) = 100\%\text{BZ}\sqrt{2^{2/3}-1}\frac{a}{\pi}\left(\frac{1-\cos(d\boldsymbol{K}_{\perp})}{a\langle\Gamma\rangle} + \boldsymbol{K}_{\perp}\tan(\theta) + \frac{1}{D_{\text{lat}}}\right). \tag{2.66}$$

Here, θ and D_{lat} denote the average mosaic angle and the average lateral grain size, respectively. An example for the oscillating FWHM in dependency of $K_{\perp}$ for a stepped surface with mosaics is shown in Fig. 2.16.
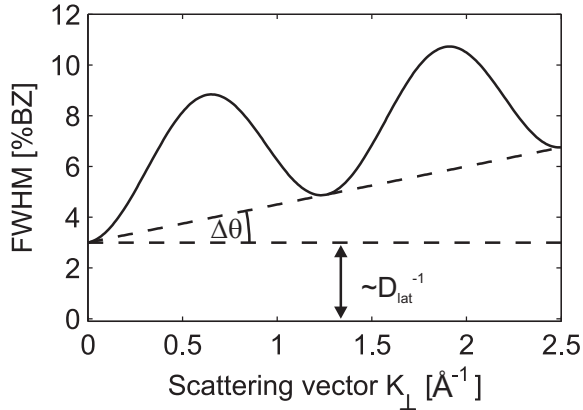

Figure 2.16: FWHM of a diffraction rod as a function of $\boldsymbol{K}_{\perp}$. The linear increase can be attributed to a mosaic spread with the average mosaic angle θ. An additional constant broadening of the spot profile is given by the grain boundaries of crystallites with the average size of D_{lat}.

2.4 Auger electron spectroscopy

Auger electron spectroscopy is a widely applied technique to obtain information about the chemical composition of surfaces. The core of this technique is the Auger effect [63] depicted in Fig. 2.17. The ionization of an atomic inner shell due to external excitation (e. g. electrons or x-rays) is followed by a recombination process of the emerging hole with a second electron from an outer shell. The released energy is either emitted as x-ray photon or a third electron from an outer shell is excited. These competitive phenomena are called x-ray fluorescence and Auger effect, respectively. Lighter elements prefer the emission of Auger electrons while x-ray fluorescence is the dominant process in heavier elements (cf. Fig. 2.18) [65]. The Auger electron is denoted by the three involved energy levels form low to high, e.g. KLM (cf. Fig. 2.17). Moreover, the Auger effect is not observed for the elements H and He since three electrons are necessary for the process.
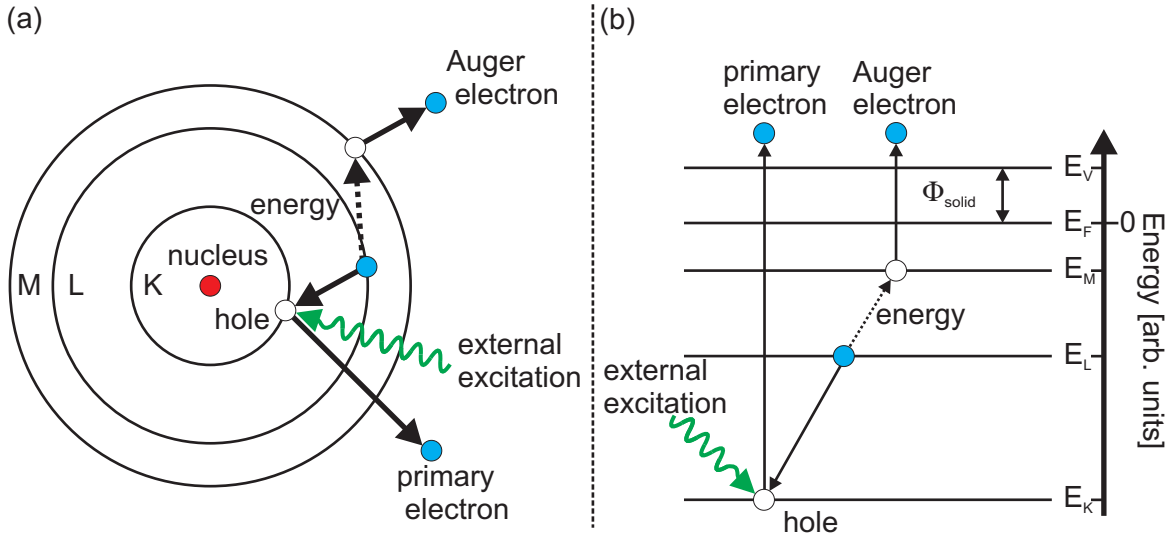
Figure 2.17: (a) Sketch of the KLM Auger process in an atom. (b) Energetic schema for a KLM transition in a solid. The degeneracy of the shells is not shown for reasons of clarity. After the inner K shell is ionized by external excitation (e.g. electrons or x-rays), the emerged hole is filled by an electron of the outer L shell. The energy generated in the process is transferred to an electron in the M shell which is released from the atom. In a solid additionally the work function Φ_{solid} between the Fermi level E_F and vacuum level E_V has to be overcome.

The kinetic energy of an Auger electron is given by the differences of the energy levels of the atom. Hence, it is independent from the primary external excitation. The characteristic position of the energy levels making Auger electron spectroscopy an element specific method. An estimation of the kinetic energies of the Auger electrons can be made with

$$E_{\text{XYZ}} = E_X - E_Y - E_Z' - U(\text{XYZ}). \tag{2.67}$$

Here X, Y and Z denote the involved shells from low to high energy level. The original energy level of the Z electron is modified by the potential of the hole in the E_V level. Moreover, the kinetic energy is influenced by the Coulomb repulsion $U(\text{XYZ})$ of the generated holes. In compounds further chemical shifts due to modified core level potentials can be observed [65].

The typical energies of the Auger electrons are in the region of 1 - 5000 eV resulting in inelastic mean free paths of a few nanometer (cf. Fig 2.10). This is the reason for the high surface sensitivity of this technique. For a quantitative analysis of Auger spectra sensitivity factors have to be used since the individual Auger transitions exhibit different probabilities. Details of quantitative analysis can be found in Ref. [66].

If electrons are used for primary excitation, it is convenient to measure the derived spectra since the signal to noise ratio is very low (cf. Sec. 4.3.2).
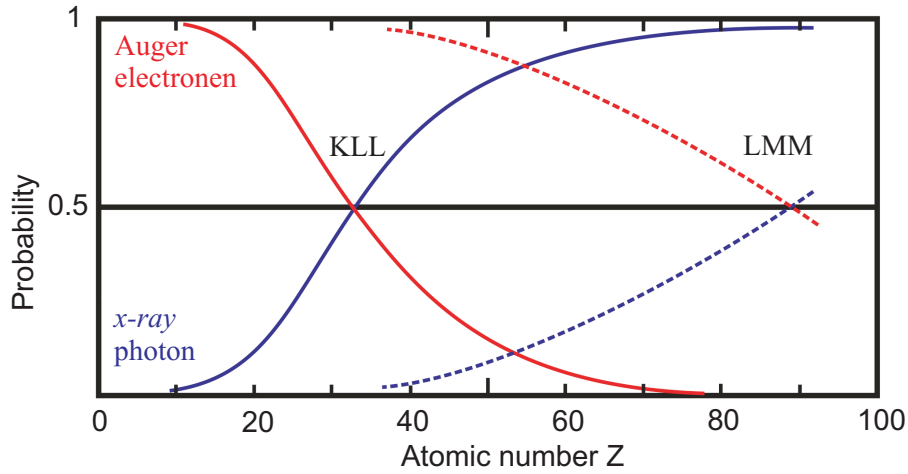
Figure 2.18: Emission probabilities of x-ray photons and of the KLL and LMM Auger electrons against atomic number. Image taken and adapted from Ref. [64].

2.5 X-ray photoelectron spectroscopy

Another powerful spectroscopic technique is the x-ray photoelectron spectroscopy (XPS). This method can be used to analyze the elemental composition of a sample. In addition, detailed information about the chemical and electronic states of the elements can be obtained [67].

XPS is based on the photoelectric effect [68–70]: Photons of an energy $h\nu$ are absorbed by the electrons of an irradiated sample. If the photon energy is higher than the ionization threshold, photo emission can be observed. The maximal kinetic energy of an emitted electron of a solid sample is given by

$$E_{\text{kin}} = h\nu - \Phi_{\text{solid}} , \tag{2.68}$$

with Φ_{solid} as the material specific work function (cf. Sec. 2.4). Equation (2.68) describes only excitation of electrons from the Fermi level E_F, stronger bound core level electrons need to overcome their binding energy E_B defined by the difference of the core level of the excited electron and the Fermi level E_F. Hence, for core level excitation the kinetic energy is given by

$$E_{\text{kin}} = h\nu - E_B - \Phi_{\text{solid}} . \tag{2.69}$$

The relationship shows that the binding energy of an electron can be evaluated if Φ_{solid} is known. For most materials the work function is difficult to determine. Conducting samples can be connected to the spectrometer results in the adjustment of the Fermi levels E_F (cf. Fig. 2.19) Here, the spectrometer acts as electron source. The work function of the emitted electrons is modified by

$$\Delta\Phi = \Phi_{\text{solid}} - \Phi_{\text{spec}} , \tag{2.70}$$

with Φ_{spec} as the work function of the spectrometer. The measured kinetic energy is now given by

$$E'_{\mathrm{kin}} = E_{\mathrm{kin}} + \Delta\Phi \tag{2.71}$$
$$= h\nu - E_{\mathrm{B}} - \Phi_{\mathrm{solid}} + (\Phi_{\mathrm{solid}} - \Phi_{\mathrm{spec}}) \tag{2.72}$$
$$= h\nu - E_{\mathrm{B}} - \Phi_{\mathrm{spec}} \tag{2.73}$$

and independent of the work function of the probed sample. Often the XPS data is presented
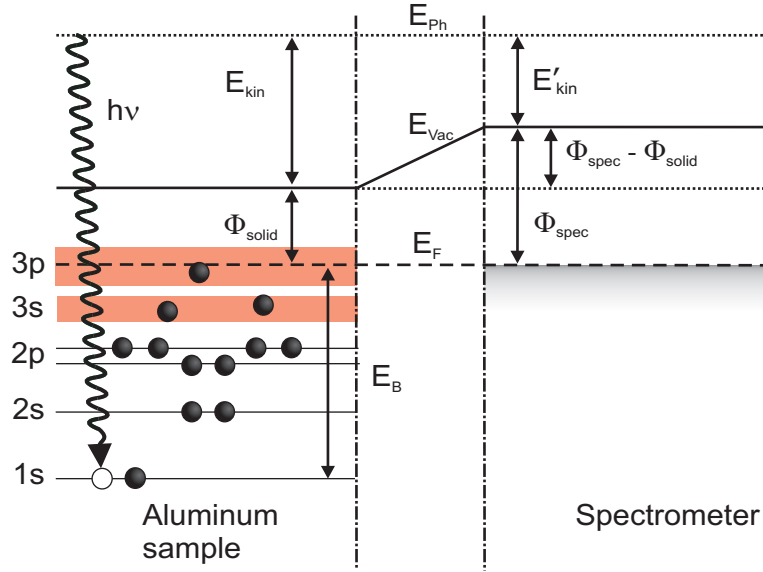

Figure 2.19: Example of XPS process using an aluminum sample. An 1s electron with the the binding energy E_{B} is rexcited from the sample due to absorption of x-rays with the energy $h\nu$. The Fermi level E_{F} of the sample and the spectrometer coincide since they are connected to each other. The binding energy E_{B} can be determined from the measured kinetic energy E'_{kin} if the work function Φ_{spec} of the spectrometer is well known (cf. Eq. (2.74)). Image taken and adapted from Ref. [71].

with the binding energy as abscissa. This is convenient since the kinetic energy of the emitted electron strongly depends on the used light source, in contrast to the binding energy which is element specific. Exceptions are emission lines caused by Auger electrons exhibiting a fixed kinetic energy (cf. Sec. 2.4). The binding energy can be determined using

$$E_{\mathrm{B}} = h\nu - E'_{\mathrm{kin}} - \Phi_{\mathrm{spec}} \,. \tag{2.74}$$

The work function of the spectrometer Φ_{spec} can easily be obtained by measuring a well known reference spectrum, e.g. Au 4f, and shifting of the spectrum, accordingly. In the case of semiconducting or isolating samples additional charging and band bending effects can

appear. The calibration of the zero point of the binding energy scale of such samples can be achieved when elements of known oxidation states are present.

The probing depth of XPS using lab x-ray sources (Al K_α = 1486.6 eV) is limited to the surface near region. Although x-rays exhibit large penetration depth in matter, the sensitivity is limited by the inelastic mean free path of the excited electrons (cf. Fig. 2.10). The kinetic energy of the emitted electrons and, therefore, the probing depth can be increased by the use of high energy x-ray sources, e.g. synchrotron radiation.

2.5.1 XP spectra

In this chapter the major features of XP spectra are briefly introduced. Note, not all of these feature, for instance satellites, can be explained solely by the photoelectric effect. A more detailed description can be found in Refs. [67, 72].

Spin orbit coupling

The nomenclature used in XP spectra is based on the quantum numbers. An emission line is identified by

$$\text{X } nl_j \, . \tag{2.75}$$

Here, X denotes the specific element and n the principle quantum number (n=1, 2, 3, ...). The number l denotes the orbital quantum number (l=0, 1, 2, 3, 4, ..., n - 1) which is labeled s, p, d, f and so on [73]. The orbital momentum l and spin momentum s ($m_s = \pm 1/2$) of a core level electron couple to the total angular momentum j. The total angular momentum of the electron is determined by

$$j = |l \pm 1/2| \, . \tag{2.76}$$

This spin orbit coupling results in doublet lines in the measured XP spectra. Only the s states (l=0) show no spin orbit coupling and, thus, can show singlet lines since j can not be negative. The intensity ratio of the doublet lines is given by

$$\frac{I_{l+1/2}}{I_{l-1/2}} = \frac{l+1}{l} \, . \tag{2.77}$$

For instance, the d level doublets (l= 2) show relative intensities of $I_{5/2}/I_{3/2} = 3/1$.

Multiplet splitting

Materials with unpaired valence electrons can show an additional spin-spin interaction due to photoelectron emission called multiplet or exchange splitting. During the photoemission process a core shell is ionized. Now the unpaired valence electrons interact through their spin with the unpaired electron in the core shell resulting in a different final state. Based on the different coupling possibilities several final states can appear resulting in complex peak structures [74]. Note, in contrast to the spin orbit splitting which is an intrinsic effect, the multiplet splitting is a final state effect caused by the photoemission process itself.

Satellites

Another feature in XP spectra due to final state effects are so called satellites. Satellite lines appear next to the core level lines and can be assigned in two classes: Intrinsic satellites are based on inter-atomic excitation while extrinsic satellites are caused by intra-atomic relaxation [75]. The origins of the satellites are the interactions between the photoemitted electron and the remaining ionized atom.

Intrinsic satellites appear if a second electron of the atom is excited. This results in an energy loss of the primary emitted electron which appears at higher binding energies in the XP spectrum due to its lower kinetic energy. The secondary electron is either transferred to a higher state or released into the continuum. The corresponding emission lines are called shake-up or shake-off satellites, respectively.

Extrinsic satellites often occur in metal oxides and are based on charge transfer effects. In the case of rare earth oxides additional satellite lines become visible in the 3d spectrum. The origin of these lines is an electron transfer from the 2p state of oxygen valence band to the 4f state of the rare earth metal ($4f^{n}v \rightarrow 4f^{n+1}\underline{v}$). The energy required for this charge transfer process is given by

$$\Delta = E(4f^{n}v) - E(4f^{n+1}\underline{v}) \, . \tag{2.78}$$

Here, $\underline{v}$ denotes a hole in the valence band. Another reason for appearance of satellites are plasmons. The kinetic energy of the photoemmited electron is lowered due to energy loss inducing a plasmon excitation. For this reason the plasmon lines are always visible at higher binding energies.

Chemical shift

Although only valence electrons of an atom participate in chemical bonds, they can have an impact on the core levels. The altered chemical environment in a compound strongly influences the Coulomb and exchange potentials. Therefore, the binding energy of the core level lines is shifted. The magnitude of these chemical shifts depends on the type of bond and can reach several eV [76]. Often it is possible to determine the oxidation state of a material from the direction and strength of the chemical shift and comparison to the pure element spectra [77].

Auger electrons

X-rays can be used to stimulate the Auger process and, thus, due to Auger electrons peaks can arise in XP spectra. The theoretical concepts responsible for their appearance are the same as described in Sec. 2.4. The kinetic energies of the Auger electrons are independent of the excitation energy. Hence, Auger peaks in XP spectra can be identified by using different excitation energies. The Auger peaks appear at different binding energies in contrast to other photoemission lines when the excitation energy is changed.

Inelastic background

If electrons are excited from deeper layers of a sample the probability of inelastic scattering processes increases. The energy loss due to these processes leads to a redistribution of the intensities in the measured XP spectra to higher binding energies forming an inelastic background. The magnitude of the energy loss is element specific and strongly depends on the kinetic energy of the excited electron (cf. Fig. 2.10).

For a quantitative analysis the inelastic background has to be subtracted. A simple approach is the description of the background with a linear function. More sophisticated background correction can be achieved by using the methods proposed by Shirley [78] or Tougaard [79].

2.5.2   3d XP spectra of the rare earth oxides

Kotani et al. [80] developed a detailed theoretical description of the photoemission process of the rare earth oxides. Following Kotani's theory the electronic structure responsible for the shape of the 3d XP spectra is briefly introduced. The appearing exchange mechanisms are exemplarily discussed for the sesquioxide phase (Ce_2O_3) of ceria (cf. Sec. 3.2). Valence band holes and core holes are denoted with $\underline{v}$ and $\underline{c}$, respectively.
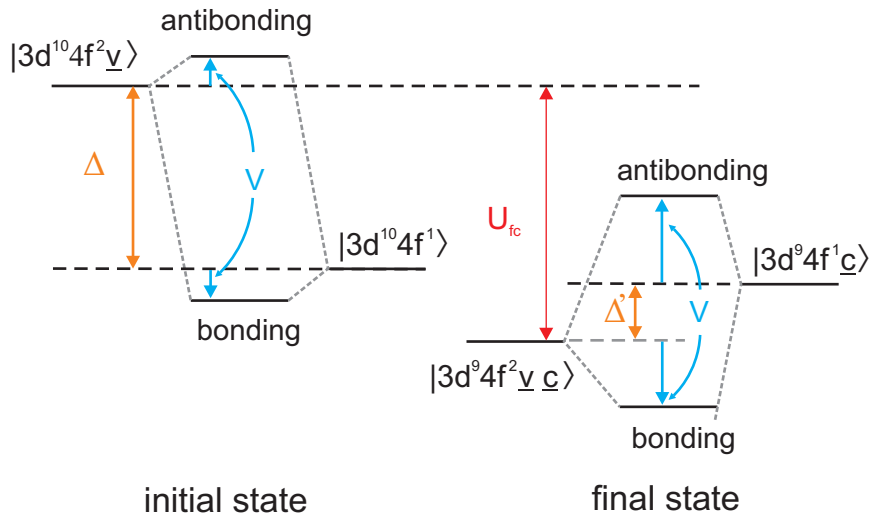

Figure 2.20: Energy schema of the initial and final state of Ce_2O_3. The system shows mainly the $3d^{10}4f^1$ configuration in the ground state due to the strong energy separation Δ and weak hybridization strength V. In the final state the energy separation Δ is lowered to Δ' by the core hole potential U_{fc}. Since Δ' and V are of the same magnitude a strong hybridization between the $|3d^94f^1\underline{c}\rangle$ and $|3d^94f^2\underline{v}\,\underline{c}\rangle$ state appears. This leads to occupation of the bonding and antibonding state resulting in two photoemission lines. Image taken and adapted from Refs. [80, 81].

In the ground state the oxygen O 2p valence band is completely filled while cerium exhibits

one electron in the Ce $|3d^{10}4f^1\rangle$ state. A weak covalency hybridization between the valence band and the $|3d^{10}4f^1\rangle$ state is present. It is possible that an electron of the valance band is transferred to the 4f level resulting in the $3d^{10}4f^2\underline{v}$ configuration and the formation of a bonding and antibonding state. However, the hybridization is negligible since the hybridization strength V is very weak in comparison with the energy separation Δ between the $|3d^{10}4f^1\rangle$ state and the valence band (cf. Fig. 2.20). Thus, mainly the $3d^{10}4f^1$ configuration is occupied.
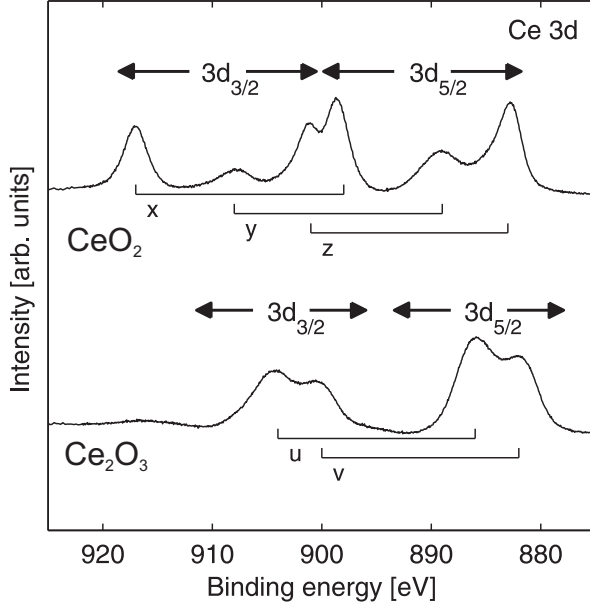

Figure 2.21: 3d XP spectra of Ce_2O_3 and CeO_2. The Ce_2O_3 spectrum shows two peaks (u, v) corresponding to the bonding and antibonding state in each $3d_{5/2}$ and $3d_{3/2}$ component. In contrast, the CeO_2 spectrum exhibits three peaks (x, y, z) in each component due to hybridized ground state.

In the final state a Ce 3d electron electron is emitted generating a hole. The now arising core hole potential lowers the energy of the 4f states by the amount U_{fc}. Since U_{fc} and Δ are of the same magnitude the energy separation becomes very small resulting in a strong hybridization of the $|3d^94f^1\underline{c}\rangle$ and $|3d^94f^2\underline{v}\rangle$ state. The bonding and antibonding states can be written as linear combinations of the $|3d^94f^1\underline{c}\rangle$ and $|3d^94f^2\underline{v}\,\underline{c}\rangle$ states which is

$$|f_1\rangle = a|3d^94f^1\underline{c}\rangle + b|3d^94f^2\underline{v}\,\underline{c}\rangle \quad \text{and} \tag{2.79}$$

$$|f_2\rangle = b|3d^94f^1\underline{c}\rangle - a|3d^94f^2\underline{v}\,\underline{c}\rangle. \tag{2.80}$$

Thus, two photoemission lines due to the bonding and antibonding state are observed in each $3d_{5/2}$ and $3d_{3/2}$ component of the 3d XP spectra (cf. Fig. 2.21).

The dioxide phase (CeO_2) of ceria exhibits, in contrast to the sesquioxide, a strongly mixed covalent ground state

$$|g\rangle = a|3d^{10}4f^1\rangle + b|3d^{10}4f^2\underline{v}\rangle. \tag{2.81}$$

This mixed ground state leads to three final states given by

$$|f_1\rangle = |3d^94f^1\underline{c}\rangle, \tag{2.82}$$

$$|f_2\rangle = c|3d^94f^2\underline{v}\,\underline{c}\rangle - d|3d^94f^3\underline{v}^2\,\underline{c}\rangle \quad \text{and} \tag{2.83}$$

$$|f_3\rangle = d|3d^94f^2\underline{v}\,\underline{c}\rangle - c|3d^94f^3\underline{v}^2\,\underline{c}\rangle. \tag{2.84}$$

Thus, each $3d_{5/2}$ and $3d_{3/2}$ component of the 3d XP spectra of CeO_2 shows three photoemission lines (cf. Fig. 2.21).

2.6 Temperature programmed desorption

Temperature programmed desorption (TPD) or thermal desorption spectroscopy (TDS) can be used to get information about the kinetic and thermodynamic properties of desorption processes. It is based on monitoring the pressure changes caused by desorbing particles in dependence of the sample temperature. In the following this technique is briefly introduced using Ref. [33] as guideline. A more detailed theoretical description can be found in Ref. [82].

TPD experiments are performed in ultra high vacuum (UHV) systems where the pressure p of the monitored species is directly proportional to the desorption rate $d\Theta/dt$. In a common TPD setup linear temperature ramps are used following

$$T(t) = T_0 + \beta t. \tag{2.85}$$

Here, t denotes the time and β the annealing rate which is usually in the magnitude of 1 - 10 K/s. Assuming identical desorption sites and no interaction between the desorbing molecules, the Polanyi-Wigner approach

$$p \propto -\frac{d\Theta}{dt} = \frac{k_n \Theta^n}{\beta} e^{-E_{des}/k_B T} \tag{2.86}$$

can be used. Here, Θ denotes the adsorbate coverage, k the desorption rate constant, n the kinetic order and k_B the Boltzmann factor. The activation energy of the desorption is denoted by E_{des}. From the equation it becomes clear that for each adsorbate a characteristic peak appears in a TPD spectrum. For low temperatures the exponential term is negligible resulting in a negligible desorption rate. At higher temperatures the desorption rate rises drastically due to the dominating exponential term. As a competitive process the adsorbate coverage Θ decreases until it vanishes and, thus, the desorption stops. Hence, a peak at a characteristic temperature can be observed in the TPD spectrum (cf. Fig. ??).

3 Investigated materials

In this chapter the investigated materials are briefly introduced. First, a short summary of the material properties of the silicon substrate is given. Afterward, the rare earth oxides ceria and praseodymia are presented. At last, the interaction between the silicon substrate and these rare earth oxides is elucidated.

3.1 Silicon

Silicon (Si) is a tetravalent element of the fourth main group of the periodic table and has the atomic number 14. It has a melting point of 1414 °C and crystallizes in the diamond structure which can be described by a non-primitive fcc lattice with a basis containing two atoms located at (0, 0, 0) and ($^1/_4$, $^1/_4$, $^1/_4$) (cf. Fig. 3.1). The lattice parameter of the cubic unit cell is $a = 5.431$ Å.
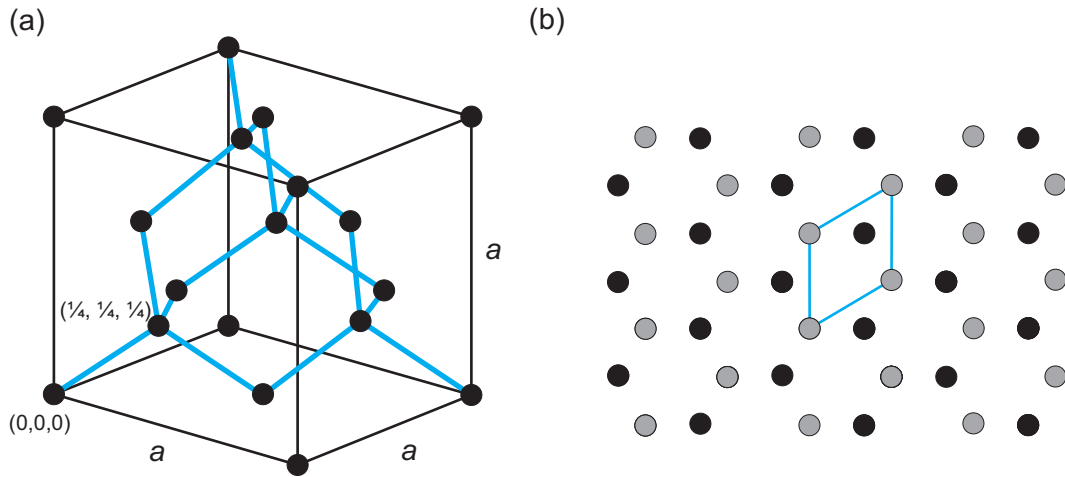

Figure 3.1: (a) Non-primitiv fcc unit cell of silicon with a lattice constant of $a = 5.431$ Å. The basis consists of two atoms located at (0, 0, 0) and ($^1/_4$, $^1/_4$, $^1/_4$). (b) Surface unit cell of the unreconstructed Si(111) surface. The atoms of the first and second layer are displayed gray and black, respectively. The hexagonal surface unit cell is marked in blue. Image taken and adapted from Ref. [61].

In microelectronics silicon of highest purity is the standard material used as substrates. It is very attractive due to its low cost and tunable electrical properties. For instance, the charge carrier concentration can be manipulated by doping with other elements, e.g. phosphor or boron. In addition, silicon offers high thermal stability of its semi-conducting properties. Furthermore, its native oxide can be used to form a sharp dielectric interface. All of these properties make silicon an ideal material for the fabrication of integrated circuits.

The unreconstructed Si(111) surface exhibits a hexagonal unit cell with a six-fold rotation symmetry using the surface normal as rotation axis. The lateral and vertical lattice constant

of the unit cell are 3.840 Å and 3.136 Å, respectively. Since the topmost atoms have different vertical positions, the six-fold rotation symmetry is reduced to a three-fold symmetry. This reduced symmetry has to be considered in the GIXRD experiments (cf. Sec. **??**).

Two main superstructures are know for the Si(111) surface. A (2×1) superstructure is observed if the samples are cleaved under UHV conditions while a (7×7) surface reconstruction can be achieved due to annealing at high temperatures. These superstructures are not further explained, since the used Si(7×7) surface structure vanishes during the growth of the rare earth films investigated in this work. A detailed description of all silicon superstructures can be found in Ref. [33].

3.2 The binary rare earth oxides

Scandium, yttrium and the lanthanides (atomic number 57 - 71) are classified as rare earth metals due to their similar chemical and physical properties. Solid state oxides with high thermal stability are formed if the rare earth metals are exposed to oxygen [23]. All rare earth oxides can be found as sesquioxide (Re_2O_3) where all cations exhibit a trivalent state (Re^{3+}). However, the formation of higher and lower oxides is possible depending on the ambient conditions since the stoichiometry is strongly influenced by the oxygen partial pressure and temperature.
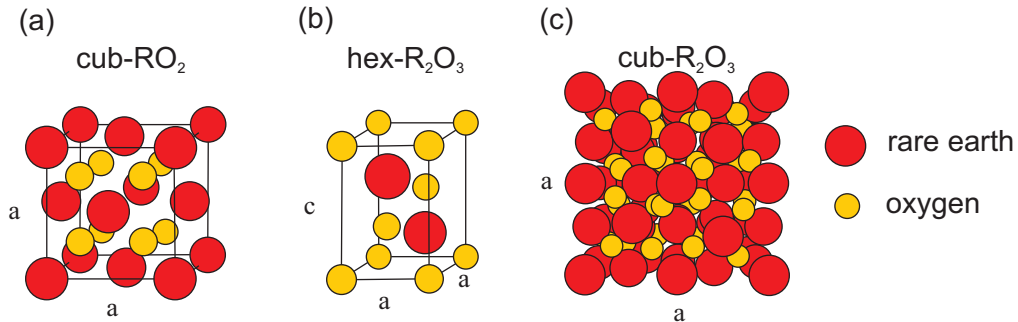

Figure 3.2: Unit cells of the rare earth oxides. (a) The dioxide phases (ReO_2) with the highest oxygen content exhibit the fluorite structure. (b) The species with the lowest oxygen content (Re_2O_3) crystallizes in a hexagonal or (c) cubic (bixbyite) structure. The structure of the cubic Re_2O_3 phase can be described by the fluorite structure exhibiting ordered oxygen vacancies. Image taken and adapted from Ref. [61].

In this work the rare earth oxides (REOs) praseodymia and ceria are investigated. These oxides, along with terbia, are the only REOs forming binary oxides (ReO_2) with all cations in the tetravalent state (Re^{4+}). In addition, several intermediate phases can be found between the dioxide ReO_2 and the sesquioxide Re_2O_3 phase. Several disordered non-stoichiometric phases as well as species with distinct stoichiometries according to a homologous series Re_nO_{2n-2m} can be observed (cf. Tab. 3.1).

The dioxide phases with the highest oxygen content exhibit the fluorite structure: The metal atoms are arranged in a fcc lattice while the oxygen atoms can be described by a primitive

Symbol	Composition	Unit cell content	n	m
ϕ	$ReO_{1.51-1.52}$	unknown	-	-
κ	$ReO_{1.65-1.67}$	unknown	-	-
σ	$ReO_{1.51-1.7}$	disordered non-stoichiometric	-	-
ι	$ReO_{1.714}$	Re_7O_{12}	7	1
ζ	$ReO_{1.788}$	Re_9O_{16}	9	1
ϵ	$ReO_{1.800}$	$Re_{40}O_{72}$ (Re_5O_9)	40	4
δ	$ReO_{1.818}$	$Re_{11}O_{20}$	11	1
β	$ReO_{1.833}$	$Re_{24}O_{44}$ (Re_6O_{11})	24	2
α	$ReO_{1.72-1.99}$	disordered non-stoichiometric	-	-

Table 3.1: Intermediate phases of the binary rare earth oxides. The stoichiometric phases can be described by Re_nO_{2n-2m}. The regions denoted by ϕ and κ are assumed single phased according to Ref. [83]. However, up to now sufficient crystallographic data is not available. Note, further polymorphic structures exist for the δ and β phase which are not listed here. Data was taken from Refs. [83, 84].

cubic sublattice (cf. Fig. 3.2). Each metal cation is coordinated by eight oxygen atoms and exhibits a Re^{4+} valence state. In contrast, the oxygen anions show a tetrahedral coordination by the metal cations.

The structures of the intermediate phases are based on the fluorite structure of the dioxide. Defects are generated in the oxygen sublattice while the fcc lattice of the cations stays more or less the same. The removal of an oxygen anions result in the formation of Re^{3+} cations. The atoms surrounding an oxygen vacancy shift slightly in their positions [84]. The metal atom move ≈ 0.2 Å away from the vacancy, while the remaining oxygen atoms shift $\approx 0.2 - 0.3$ Å towards the vacancy. Thus, the vacancy exhibit a slightly positive charge. Since the basic fluorite structure is only slightly distorted, pseudo-cubic lattice parameter can be assigned to the intermediate phases [85–87]. These pseudo-cubic lattice parameter increase linear with decreasing oxygen content due to expansion of the cations radii and can be used to estimate the stoichiometry of the intermediate phases (cf. Sec. ??).

The intermediate phases of the homologous series with high defect concentration (ι, ζ and ϵ) show paired defects [84]. These defects are aligned along the body diagonal of the oxygen sublattice. In contrast, the phases with low defect concentration (δ and β) form isolated defects with large defect separation.

The sesquioxide marks the species with the lowest oxygen content and can be found in five polymorph configurations. The most common configuration is the bixbiyte structure which is directly related to the fluorite structure of the dioxide. The unit cell can be constructed by doubling of the fluorite lattice constant and removing one fourth of the oxygen atoms (cf.

Fig. 3.2). The oxygen vacancies are formed along non-intersecting strings in the four $\langle 111 \rangle$ directions. The metal atoms are coordinated by six oxygen atoms and exhibit a Re^{3+} valence state while the oxygen atoms are still tetrahedral coordination by the metal cations.

Another important configuration is the hexagonal structure which is usually stabilized at high temperatures. Here, the unit cell is much smaller and contains only two metal cations and three oxygen anions (cf. Fig. 3.2). The metal atoms are coordinated by seven oxygen atoms due to the tetrahedral and octahedral stacking of the oxygen layers. The other polymorph configuration of the sesquioxide are not relevant for this work and will not be discussed any further. Detailed information can be found in Ref. [84].
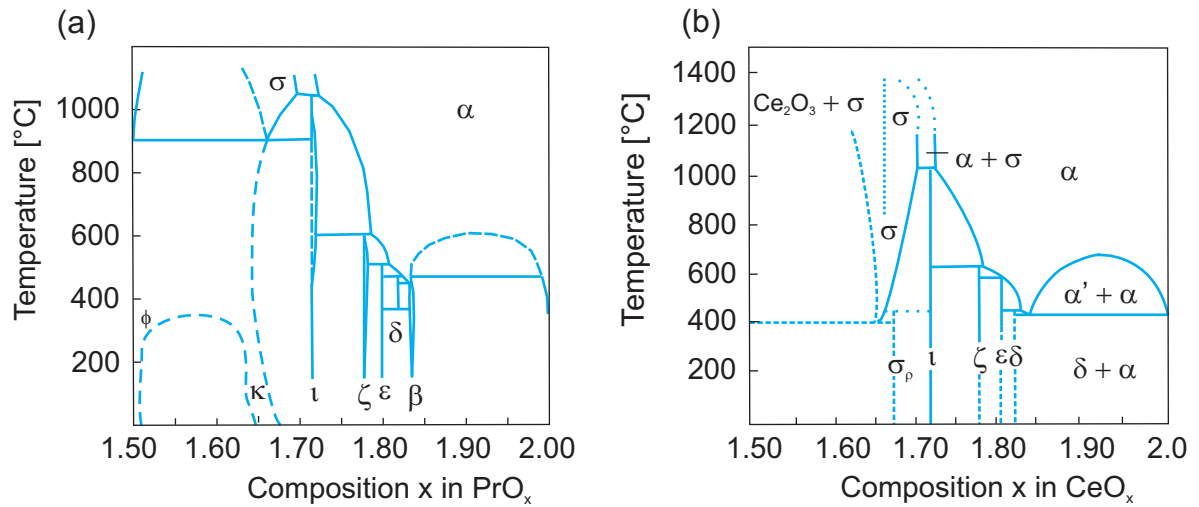
Figure 3.3: Partial phase diagram of bulk praseodymia (a) and ceria (b). The equilibrium stoichiometries strongly depend on temperature and oxygen ambient pressure. A list of the intermediate phases can be found in Tab. 3.1. Image taken and adapted from Ref. [84].

3.3 Praseodymia on Si(111)

In this thesis praseodymia films grown on Si(111) by molecular beam epitaxy (MBE) are investigated. In the following an overview of previous studies concerning this topic is given.

Schroeder et al. [13, 14] have shown that single crystalline hex-Pr_2O_3(0001) films of high quality can be grown on Si(111) using a substrate temperature of 625°C and high deposition rates (6 nm/min). Furthermore, it was revealed by transmission electron microscopy (TEM) that these films exhibit a sharp interface of high thermal stability between the oxide film and the substrate [15, 16]. Later Schaefer et al. [88] demonstrated that the deposition rate is a crucial factor for the epitaxial growth since lower rates (0.06 nm/min) lead to the formation of praseodymium silicide and silicate.

The hex-Pr_2O_3(0001) films can be transformed to cub-Pr_2O_3(111) phase by annealing in 10^{-5} mbar oxygen [15] or 1 bar nitrogen [16] atmosphere at 600°C and 700°C, respectively. The cub-Pr_2O_3(111) films are twin free and exhibit an exclusive B-type orientation which

means they are rotated 180° with respect to the substrate. During the phase transition an amorphous silicate interface layer is formed containing a Pr-rich part close to the oxide and an SiO_2-rich part close to the substrate. This interface is undesired from the application point of view [28] and its formation can be significantly suppressed by the use of chlorine passivated substrates as demonstrated in Ref. [89].

Higher oxidized films with stoichiometries close to PrO_2 can be achieved by post deposition annealing (PDA) in oxygen atmosphere. Weisemoeller et al. [29,90] performed a detailed PDA study using temperatures of 300°C - 700°C and 1 bar oxygen atmosphere. It was shown that the oxidized films contain two lateral coexisting oxide species which can be described by a two column model. Also a lateral pinning of the cubic films close to the lateral lattice constant of hex-$Pr_2O_3(0001)$ was observed. In addition, they reported the growth of the amorphous interface with increasing PDA temperature.

Gevers et al. [91] confirmed the two column model in a PDA study of pre-oxidied $PrO_2(111)$ films. It was also shown that the lateral pinning of the films results in tetragonal distortion. The induced stress is partially released during the reduction by the formation of mosaics which was deduced from SPA-LEED and XRD measurements.

Recently it was shown that $PrO_2(111)$ films with clean surfaces and true stoichiometry can be achieved by exposure to cold oxygen plasma [92]. In contrast to oxidation by PDA, this method does not increase the interface thickness during the oxidation process as shown in Ref. [93].

3.4   Ceria on Si(111)

In contrast to praseodymia, ceria crystallizes as $CeO_2(111)$ on Si(111) if deposited via MBE [94, 95]. Epitaxial growth of single crystalline films can be achieved using growth rates of 0.004 nm/s - 0.011 nm/s and substrate temperatures in the region of 175°C - 800°C. Several similarities to the cubic praseodymia films were found. For instance, Nagata et al. [96] have shown that the $CeO_2(111)$ films prefer B-type orientation similar to cubic praseodymia. Furthermore, a comparable amorphous silicate interface is formed during the growth which consists of a Ce-rich part close to the oxide and an SiO_2-rich part close to the substrate [30,97].

Only a limited number of studies addressing reduced ceria films on Si(111) can be found in literature since thermal treatment results in an undesired interface growth. Flege et al. [98] proposed an alternative growth method by combining reactive growth with chlorine passivated substrates. Cerium metal was evaporated in diluted oxygen atmosphere leading to the growth of cubic $Ce_2O_3(111)$ films with excess oxygen. They demonstrated by x-ray standing waves (XSW) measurements that the interface is atomically sharp. In addition, it was shown that the films can be further oxidized to CeO_2 by exposure to ambient condition while the sharp interface stays intact. However, a detailed study addressing the thermal stability of these films is not available up to now.

Another approach is presented in Ref. [99] using the reactive growth method and a CaF_2 buffer layer. The authors have shown that the interface formation during growth is suppressed. Unfortunately, these films show only limited thermal stability due to interdiffusion of fluorine into the ceria film at elevated temperatures.

Recently, Zoellner et al. [100] demonstrated that twin free $CeO_2(111)$ films with B-type orientation can be grown with MBE on hex-Pr_2O_3/Si(111) and cub-Pr_2O_3/Si(111) buffer layers. In this thesis the thermal stability of these $CeO_2(111)$/hex-Pr_2O_3/Si(111) system is explored.

4 Experimental setup

In this chapter an introduction of the sample preparation and used experimental setups is given. First, the sample preparation is described, afterward, the synchrotron based XRD and GIXRD as well as the surface science experiments are presented.

4.1 Sample preparation

The samples investigated in this thesis were prepared by the IHP GmbH in Frankfurt (Oder). Single crystalline Si(111) wafer with a diameter of 4" and a thickness of (525 ± 15) μm were used as substrates. The surface exhibits a miscut of $(0.35 \pm 0.15)°$ mainly at the $[1\bar{1}0]$ direction resulting in a mean terrace width of 36 - 90 nm. Furthermore, the substrates show a resistivity of 5 - 15 Ωcm due to a slight boron doping. The wafer were cleaned before the growth process using a standard wet-etching technique. A detailed description of the cleaning procedure can be found in Refs. [13, 101]. Afterward the samples were loaded into the UHV chamber depicted in Fig. 4.1.
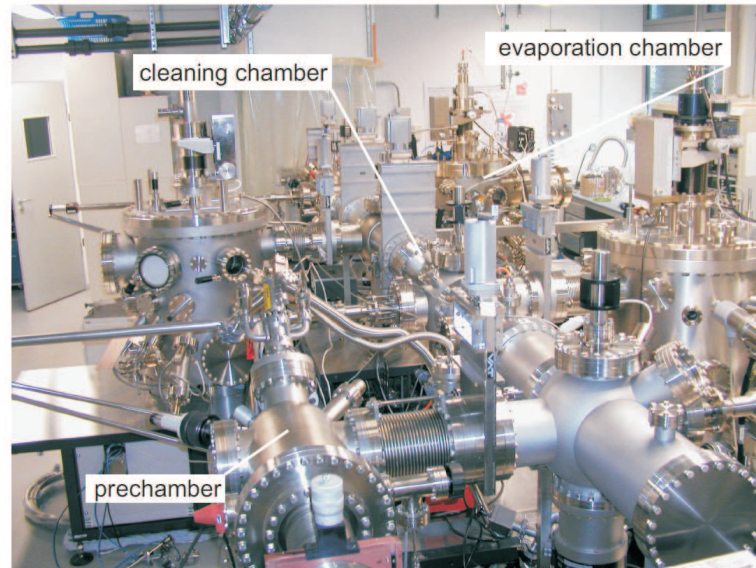
Figure 4.1: MBE growth setup at the IHP in Franfurt (Oder). The investigated films were prepared in the evaporation chamber. Image taken from Ref. [61].

The samples and the sample holder were degassed at 200°C for 30 min in the prechamber. Thereafter, they were transferred to the cleaning chamber and annealed at 700°C resulting in a high quality Si(111)(7 × 7) surface, which was monitored by LEED. The praseodymia and ceria films were grown with a molecular beam epitaxy (MBE) system of the type DCA 600 in the evaporation chamber. In this setup, praseodymia and ceria powder placed in a crucible is directly annealed to evaporation temperature using a focused electron beam.

The powders used for the film growth were Pr_6O_{11} and CeO_2 which are the stable configurations of these REOs at ambient conditions. The growth rate for the praseodymia and ceria films was adjusted to 3 nm/min and the substrate temperature was set to 625°C. To prevent inhomogeneous growth of the films the substrate was rotated during evaporation. In contrast to ceria, which is deposited as CeO_2, praseodymia is reduced to Pr_2O_3 during the evaporation process.

The praseodymia films grown in this manner exhibit a high quality twin-free hex-$Pr_2O_3(0001)$ structure as shown in Ref. [14]. In this thesis the surface morphology of the hex-$Pr_2O_3(0001)$ films was investigated (cf. Sec. 5). Therefore, the samples must be transferred through ambient conditions from the growth chamber to the surface analysis chamber located in Frankfurt and Osnabrück, respectively. The transfer of the samples is problematic since hex-$Pr_2O_3(0001)$ tends to form hydroxides $(Pr(OH)_3)$ at ambient conditions [102, 103], thus, suitable capping layers are needed. For this thesis amorphous germanium films were used since they can be easily removed by annealing in oxygen atmosphere (cf. Sec. **??**). These films were grown using MBE while the substrate was kept at room temperature.

For the studies presented in Sec. 6 the hexagonal Pr_2O_3 films were further oxidized in two steps. First, the samples were transferred ex-situ into an oven and annealed for 30 minutes at 450°C at 1 bar oxygen atmosphere and constant gas flow. This treatment leads to slightly reduced $PrO_2(111)$ films with fluorite structure as shown in Refs. [29, 101]. Furthermore, an additional plasma treatment is necessary to obtain stoichiometric $PrO_2(111)$ films [92, 93]. This second step was done at the IACP in Bremen using an in-situ radio-frequency (RF) plasma source. The parameters used for the plasma treatment were 9 mbar oxygen partial-pressure, 15 sccm (standard cubic centimeter per minute) constant gas flow, 30 W power and an exposure time of 60 minutes. A detailed description of the used plasma setup can be found in Ref. [104].

The investigated $CeO_2(111)$ films were grown on a hex-$Pr_2O_3(0001)$ buffer layer using the parameters described above. The growth of the buffer layer was monitored via reflection high-energy electron diffraction (RHEED) and the deposition was stopped after complete coverage of the Si(111) substrate was reached (thickness $\approx$ 3 nm). Furthermore, prior to the surface investigations the $CeO_2(111)$ samples were exposed to an in-situ oxygen microwave plasma (2.45 GHz) for 15 minutes to clean the surface and lower the oxygen defect density. The used plasma parameters were 80 sccm gas flow, 0.26 mbar oxygen pressure and 360 W power. A detailed description of the used plasma setup can be found in Ref. [105].

4.2 XRD and GIXRD

The x-ray diffraction experiments presented in this work have been carried out at the second and third generation synchrotron radiation source DORIS III and PETRA III located at HASYLAB/DESY. These radiation sources offer several advantages in comparison with conventional laboratory sources. The high intensities and high resolution make them a perfect tool for the investigation of thin film systems.
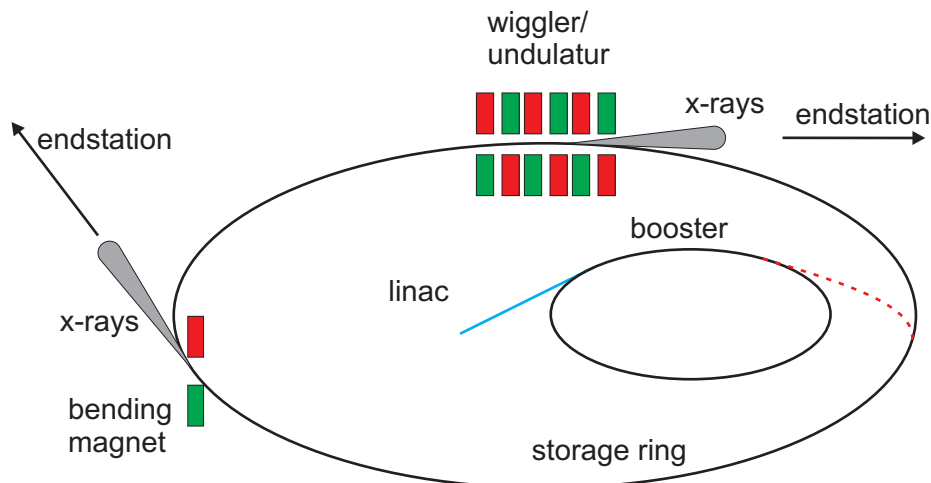

Figure 4.2: Sketch of a synchrotron facility. Prior to the injection of the electrons or positrons into the storage ring, they are accelerated at the linear accelerator (linac) and booster ring. At the storage ring bending magnets, wigglers or undulators are used to generate the radiation for the experimental endstations.

In general a synchrotron facility consists of three major parts: the linear accelerator, the booster and the storage ring. In the linear accelerator or linac charged particles (electrons or positrons) are accelerated to a velocity close to the speed of light. Afterward, the particles are injected into a ring shaped accelerator called booster. This is necessary since the energy upkeep at the linac is limited by its length scale. At the booster the velocity of the particles is further increased to the targeted energy using radio frequency cavities. Thereafter, the particles are inserted into the storage ring where they are kept at constant speed. The particles within the storage ring exhibit an altered radiation field due to their relativistic velocity. Non-relativistic particles at a curved trajectory exhibit a toroidal shaped dipole field with the main axis in the direction of the accelerating force (cf. Fig. 4.3). In contrast, the particles with relativistic velocities show a cone shaped field pointing in the direction of particle propagation.

The radiation needed for the experiments is generated by manipulation of the path of the particles. The devices used for the purpose are bending magnets, wigglers or undulators.

The bending magnets are used to keep the particles at the circular trajectory. The particles are accelerated due to Lorentz force which results in the emission of radiation. The emitted energy spectrum is continuous and depends on the bending radius of the magnet which is
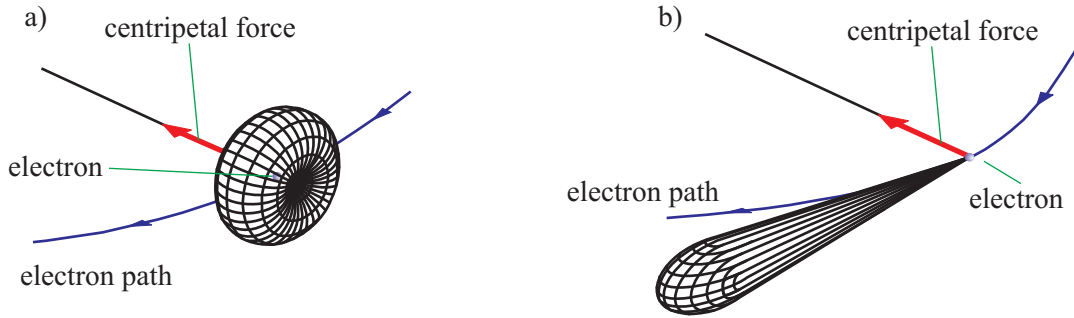
Figure 4.3: Radiation field of electron at a curved trajectory: (a) non-relativistic velocity (b) relativistic velocity. Image taken and adapted from Ref. [106].

limited by the ring geometry.

Higher intensities and smaller divergence of the x-ray beam can be achieved by the use of alternating magnets which are periodically arranged. The particles exhibit an oscillating trajectory within these arrays of magnets. Dependent on the displacement of the particles from their ideal path the device is called wiggler or undulator. Particles passing through a wiggler exhibit a large displacement which results in an incoherent superposition of the emitted radiation. Thus, a continuous spectrum similar to the spectrum of a bending magnet can be observed. In contrast, the particles passing through an undulator show only a small deviation from the ideal trajectory. The displacement is so adjusted that the emitted radiation is superimposed coherently which results in sharp emission lines. The intensity gain scales linear and quadratic with the number of periods for wigglers and undulators, respectively. A more detailed description of the mentioned devices can be found in Ref. [107].

The two x-ray diffraction beamlines W1 and BW2 at the DORIS III synchrotron are equipped with a wiggler of 16 and 28 periods, respectively. The BW2 beamline exhibits a higher intensity due to its larger number of wiggler periods. The continuous radiation spectrum of the wiggler is filtered by a double-crystal Si(111) monochromator: Two parallel Si(111) crystals are tilted to fulfill the Bragg condition for a specific energy. Thus, only photons of that energy can pass through the monochromator. Gold coated mirrors are used to focus the beam on the sample position and to suppress higher harmonics. The shape of the x-ray beam is defined by a four slit system. For the experiments presented in this thesis photon energies of 10.5 keV are used at W1 and 10 keV at BW2 corresponding to wavelengths of 1.18 Å and 1.24 Å, respectively.

The beamline P08 at the third generation synchrotron PETRA III exhibit a significant higher intensity and resolution as the beamlines described above [108]. Next to the higher intensity generated by the synchrotron itself an undulator of 67 periods is used. Based on the experimental circumstances two monochromators are installed at P08. The first one is a double-crystal Si(111) monochromator similar to the ones equipped at W1 and BW2, while the second one is a large offset monochromator (LOM) used to suppress higher harmonics and separate the beams of P08 and its adjacent beamline P09. Compound refractive beryllium lenses (CRLs) are used to focus and collimate the beam. Similar to BW2 a photon energy of

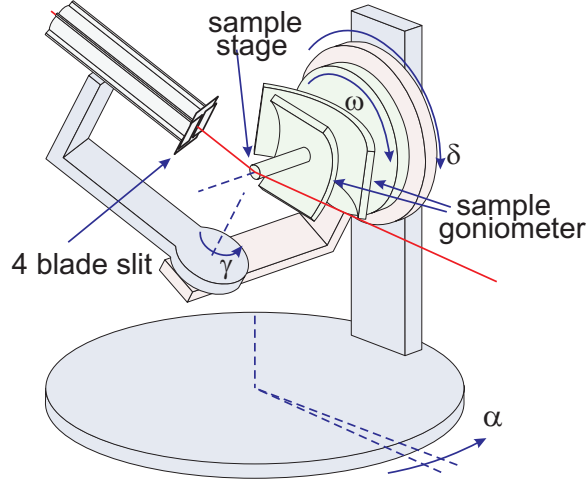10 keV is used for the experiments and a slit system defines the beam shape. At all beam-

Figure 4.4: Sketch of the six-circle diffractometer used at the beamlines W1 and BW2. The detector position is defined by the angles γ and δ while the whole diffractometer can be rotated by α. The surface of the sample is aligned with the goniometer and can be rotated with ω. The 4 blade slit system is used to suppress background scattering. Image taken from Ref. [46].

lines the actual experiments are performed with six-circle diffractometers equipped with a Si-strip line-detector (MYTHEN) [109]. Furthermore, a primary beam intensity monitor and a beam attenuator are installed since the detector would be damaged if exposed to radiation with high intensity. In front of the detector an additional slit system is installed to suppress background scattering. The beamlines W1 and BW2 are equipped z-axis diffractometer (cf. Fig. 4.4) while the beamline P08 exhibits a 4S+2D type diffractometer. Two different modes were used for the XRD and GIXRD measurements which are discussed exemplary for the W1/BW2 setup in the following.

The diffractometer used at W1/BW2 is depicted at Fig. 4.4. In the setup the whole diffractometer can be tilted with respect to the incidence beam by the angle α. The sample is located at the pivot point of the diffractometer and the surface of the sample is aligned with a goniometer. Rotation of the sample is given by ω while the detector position is defined by the angles γ and δ.

For the XRD measurements of the specular diffraction rod the horizontal mode was used where the angles γ and α are kept at zero. The sample is horizontally mounted so that the surface normal defined by the crystal planes is parallel to the incidence plane of the x-rays. The incidence angle is now defined by ω while the diffraction angle is given by δ. If the incidence angle ω is now tilted by value θ, the diffraction angle δ has to be rotated by the value 2θ to fulfill the scattering conditions.

The GIXRD measurements were performed in the vertical mode. Here, the sample is vertically mounted with the surface normal of the crystal planes perpendicular to the incident plane. In this setup a fixed incident angle is used which is now defined by α. The angle ω can be

used to rotate the sample 360° with the surface normal as rotation axis. The sample rotation in combination with the detector angles γ and δ gives access to in-plane Bragg peaks as well as higher order diffraction rods.

4.3 UHV setups

In this section the experimental setups of the surface science methods are introduced. All measurements were performed in ultra high vacuum chambers (bases pressure 10^{-10} mbar, each).

The SPA-LEED, AES and XPS measurements were carried out in Osnabrück using two different UHV systems. The first chamber is equipped with the SPA-LEED and AES system and annealing of the samples is realized with resistive heating. The second chamber was used for the XPS measurements. Here, the sample heating was realized with electron bombardment. Detailed information about the first and second chamber can be found in Refs. [61, 110, 111] and Refs. [71, 112, 113], respectively.

The TPD experiments were carried out using a third chamber at the IAPC in Bremen. A quadrupol mass spectrometer was used to detect the desorbing oxygen and sample annealing was realized with electron bombardment similar to the heating in the XPS chamber. More information about the TPD setup can be found in Ref. [114].
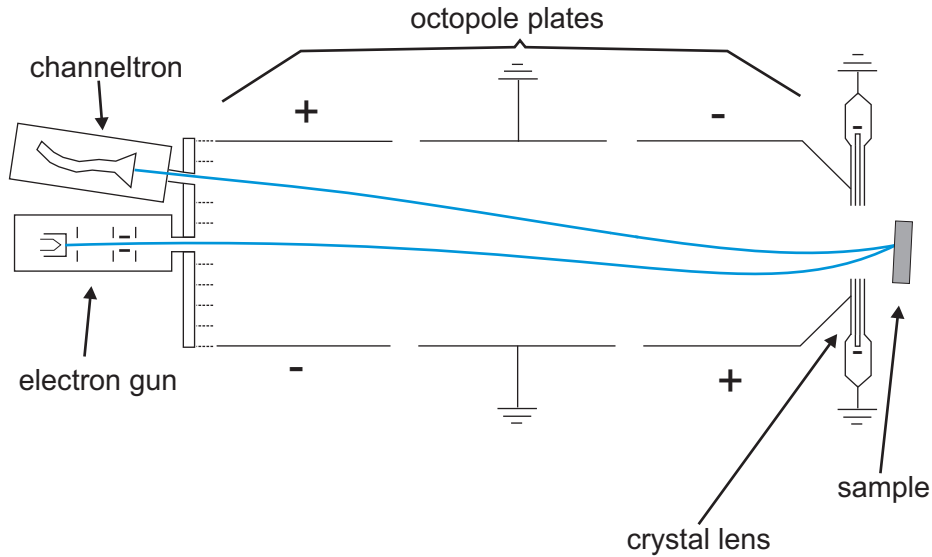
Figure 4.5: Sketch of the SPA-LEED instrument. Electrons are accelerated by the electron gun and focused at the channeltron detector using the lens system. The incidence angle of the electron beam is varied using the electric octopole field. Image taken and adapted from Ref. [115].

4.3.1 SPA-LEED

The SPA-LEED instrument was developed by Henzler et al. [116] enabling the measurement of high resolution electron diffraction pattern and the analysis of spot profiles. For this thesis a second generation Leybold system was used which is sketched in Fig. 4.5. The system contains four major parts: The electron gun, the lens system, the octopole and a channel electron multiplier (channeltron) as the detector.

An electron beam with an energy up to 500 eV is emitted from the electron gun. The beam passes twice through the octopole system on its way to the detector causing a deflection of the electrons. Two electrostatic lenses located at the exit of the electron gun and in front of the sample are used to focus the diffracted beam on the detector. The electric field of the octopole is used to vary the incidence angle of the beam, while the angle between incoming and diffracted beam is kept constant. Thus, the reciprocal space can be scanned laterally.

The SPA-LEED has several advantages in comparison with a conventional LEED setup [33]. Due to the varying incident angle a larger section of the reciprocal space is detected. Furthermore, the specular diffraction spot is accessible which is covered by the electron gun in a conventional setup. Using spot profile analysis not only the structure but also the morphology of surfaces can be investigated. This features in combination with the high resolution and digital data acquisition make the SPA-LEED a perfect tool for surface analysis.
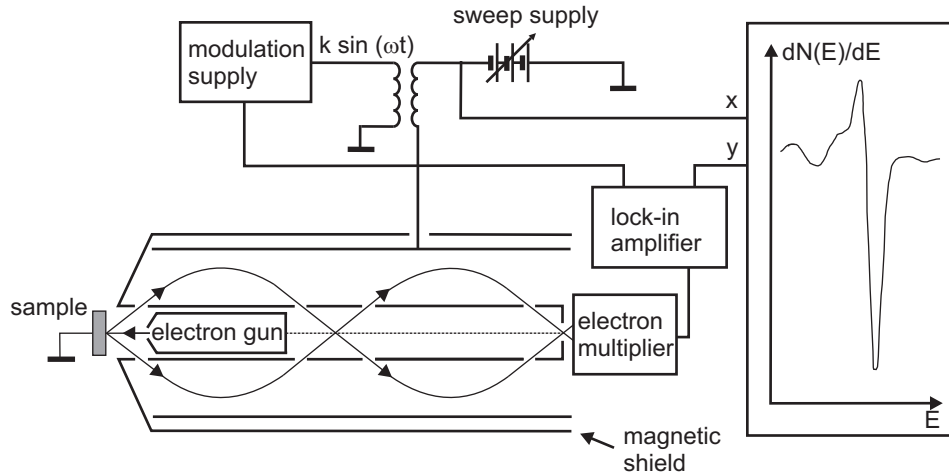
4.3.2 AES

Figure 4.6: Sketch of a typical AES setup. Auger electrons are excited using an electron gun. The emitted electrons pass through the cylindrical mirror analyzer (CMA) and are detected with the electron multiplier. Due to high background intensities, derived spectra are measured. Image taken and adapted from Ref. [33].

In this work an Auger electron spectrometer of the type PHI 10-155 equipped with a cylindrical mirror analyzer (CMA) was used. A typical AES setup using a CMA is depicted in

Fig. 4.6. The electron gun accelerates electrons with an energy of 3 - 5 keV onto the sample. Here, Auger electrons are excited and travel into the cylindrical mirror analyzer.

The CMA consists of two concentric cylinders with the same axis. The inner cylinder exhibits several gaps and a voltage is applied between the two cylinders. Due to this setup the cylinders become an energy filter. Only electrons exhibiting the right pass energy can reach the electron multiplier. If the electrons are to slow or to fast, they will hit the inner or outer cylinder, respectively. An energy dependent spectrum can be measured by sweeping the applied voltage.

It is suitable to measure derived spectra since the Auger peaks are superimposed with a large background signal. For this reason, the sweep voltage is superimposed with a small a.c. voltage and the multiplier is connected to a lock-in amplifier.

4.3.3 XPS

A commercial SPECS system was used for the XPS measurements. The setup is sketched in Fig. 4.7 and consists of four major parts: the x-ray source, the lens system, the concentric hemispherical energy analyzer and the detector. The non-monochromatic source of the type
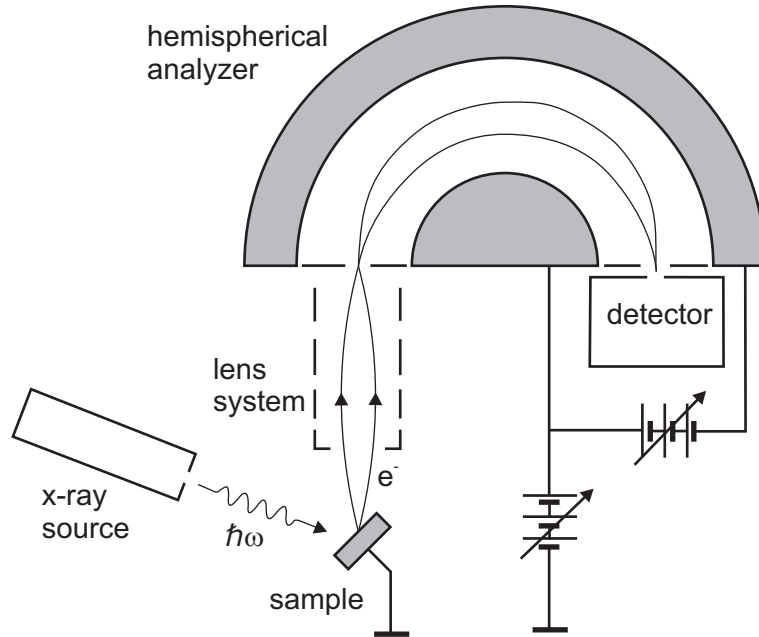
Figure 4.7: Sketch of the used XPS setup. By irradiation of the sample with x-rays photoelectrons are emitted. The lens system focuses the electrons on the analyzer entrance. Only electrons with the right path energy can pass the concentric hemispherical analyzer (CHA) and reach the detector. Image taken and adapted from Ref. [33].

SPECS XR 50 is equipped with a twin anode. Either an aluminum or magnesium anode can be used which irradiate photons of the energy Al K_α= 1486.6 eV and Mg K_α = 1253.6 eV, respectively. For the presented studies only the aluminum anode is used.

The photoelectrons emitted from the sample propagate through a lens system into the concentric hemispherical analyzer (CHA) of the type PHOIBOS 150. The CHA consists of two concentric hemispheres between which a voltage is applied. Due to this setup only electrons exhibiting the right pass energy can reach the detector. The detector consists of an array of six channel electron multiplier. Similar to the CMA (see Sec. 4.3.2) electrons with too low or too high energy are deflected on one of the hemispheres.

The lens system focuses the electrons on the analyzer entrance and is used to optimize the imaging properties of the detector. Furthermore, this system is designed to retard the electrons entering the analyzer enabling two operation modes.

The first mode is called fixed analyzer transition (FAT) and offers the advantage of a constant energy resolution ΔE. In this mode the pass energy of the analyzer is kept constant while the retardation is swept. The FAT mode is usually the standard mode for XPS measurements

In the second mode, which is called fixed retarding ratio (FRR), the retardation is kept constant and the pass energy is swept. Here, the resolution scales with electron energy ($\Delta E/E = $ const.). This mode can be used to resolve broad peaks of little intensity at low kinetic energies.

Surface morphology of ultrathin hex-Pr$_2$O$_3$ films on Si(111)

H. Wilkens*, J. Rodewald*, S. Gevers*, M. H. Zoellner**, T. Schroeder**,*** and J. Wollschläger* [†]

* Department of Physics, University of Osnabrück, Barbarastrasse 7, D-49069 Osnabrück, Germany
** IHP, Im Technologiepark 25, D-15236 Frankfurt(Oder), Germany
*** BTU Cottbus, Institute of Physics, Konrad-Zuse-Str.1, D-03046 Cottbus, Germany

Abstract

In this work the morphology of the surface of hexagonal Pr$_2$O$_3$(0001) films grown on Si(111) is studied by high resolution low energy electron diffraction combined with spot profile analysis. For this purpose, praseodymia films prepared by molecular beam epitaxy were capped with protecting amorphous germanium films. After removal of the capping layers due to heating in diluted oxygen atmosphere the surface properties of the oxide film were investigated in-situ with Auger electron spectroscopy and spot profile analysis low energy electron diffraction. The removal of the capping layer has no impact on the hexagonal Pr$_2$O$_3$(0001) film structure which is shown by x-ray diffraction. Surface sensitive electron diffraction confirms that the surface of the oxide film has hexagonal structure. Diffraction spot profile analysis shows that the film surface has grain structure without any mosaic spread due to the negligible lateral lattice mismatch between hexagonal Pr$_2$O$_3$(0001) and Si(111). In addition, single atomic steps with complete bulk unit cell height are present at the surface. The density of the atomic steps is small pointing again to the high quality of the surface of hexagonal Pr$_2$O$_3$ films compared to cubic Pr$_2$O$_3$ films.

[†]Electronic mail: joachim.wollschlaeger@uos.de

Structural changes of ultra thin cub-PrO$_2$(111)/Si(111) films due to thermally induced oxygen desorption

H. Wilkens*, S. Gevers*, S. Röhe**, A. Schaefer**, M. Bäumer**, M. H. Zoellner***, T. Schroeder***,**** and J. Wollschläger* ‡

* *Department of Physics, University of Osnabrück, Barbarastrasse 7, D-49069 Osnabrück, Germany*
** Institute of Applied and Physical Chemistry, University of Bremen, Leobener Str. NW2, D-28359 Bremen, Germany
*** IHP, Im Technologiepark 25, D-15236 Frankfurt(Oder), Germany
**** BTU Cottbus, Institute of Physics, Konrad-Zuse-Str.1, D-03046 Cottbus, Germany

Abstract

The structural changes of ultra thin PrO$_2$(111) films grown on Si(111) due to thermal reduction in ultra high vacuum are investigated. Therefore, praseodymia films are treated with oxygen plasma to obtain completely oxidized PrO$_2$ films. The reduction of these films is studied with thermal desorption spectroscopy combined with *ex-situ* x-ray diffraction measurements. It is shown that the distinct desorption peaks of molecular oxygen are correlated with stabilization of several intermediate phases of praseodymia. The most intense signal of desorbing oxygen is observed at $\approx$ 650 K. It is coupled to the strongest impact on the crystalline structure since we observe the transition PrO$_2 \rightarrow$Pr$_5$O$_9$. Further oxygen desorption leads to additional phase transitions with laterally coexisting phases. Grazing incidence x-ray diffraction measurements reveal that the initial pinning to the lateral lattice constant of hexagonal Pr$_2$O$_3$(0001) is not breached due to the plasma treatment. This hexagonal pinning is released during the oxygen desorption so that the crystalline structure of the praseodymia films does not only expand vertically but also laterally.

---

‡Electronic mail: joachim.wollschlaeger@uos.de

Stabilization of the ceria ι-phase (Ce_7O_{12}) surface on Si(111)

H. Wilkens[*], O. Schuckmann[*], R. Oelke[*], S. Gevers[*], A. Schaefer[**], M. Bäumer[**], M. H. Zoellner[***], T. Schroeder[***],[****] and J. Wollschläger[*] [§]

[*] *Department of Physics, University of Osnabrück, Barbarastrasse 7, D-49069 Osnabrück, Germany*
[**] Institute of Applied and Physical Chemistry, University of Bremen, Leobener Str. NW2, D-28359 Bremen, Germany
[***] IHP, Im Technologiepark 25, D-15236 Frankfurt(Oder), Germany
[****] BTU Cottbus, Institute of Physics, Konrad-Zuse-Str.1, D-03046 Cottbus, Germany

Abstract

In this work a 250 nm $CeO_2(111)$ film grown on a hex-$Pr_2O_3(0001)$/Si(111) system is annealed at 660°C for 30 min to stabilize the (111) surface of the ι-phase (Ce_7O_{12}). The structural characterization of the $Ce_7O_{12}(111)$ surface is performed via SPA-LEED. The ι-phase surface exhibits a $(\sqrt{7}x\sqrt{7})R19.1°$ superstructure with two mirror domains which can be attributed to a periodic ordering of oxygen vacancies in the fluorite structure. Also the stoichiometry is confirmed by XPS due to a factor analysis of the Ce 3d spectra.

[§]Electronic mail: joachim.wollschlaeger@uos.de

Structural transitions of epitaxial ceria films on Si(111)

H. Wilkens*, O. Schuckmann*, R. Oelke*, S. Gevers*, M. Reichling* A. Schaefer**, M. Bäumer**, M. H. Zoellner***, T. Schroeder***,**** and J. Wollschläger* ¶

* *Department of Physics, University of Osnabrück, Barbarastrasse 7, D-49069 Osnabrück, Germany*
** Institute of Applied and Physical Chemistry, University of Bremen, Leobener Str. NW2, D-28359 Bremen, Germany
*** IHP, Im Technologiepark 25, D-15236 Frankfurt(Oder), Germany
**** BTU Cottbus, Institute of Physics, Konrad-Zuse-Str.1, D-03046 Cottbus, Germany

Abstract

The structural changes of a (111) oriented CeO_2 film grown on a hex-$Pr_2O_3(0001)$/Si(111) system due to post deposition annealing are investigated. X-ray photoelectron spectroscopy measurements revealing the near surface stoichiometry show that the film reduces continuously upon extended heat treatment. The film is not homogeneously reduced since several coexisting crystalline ceria phases are stabilized due to subsequent annealing at different temperatures as revealed by high resolution low energy electron diffraction and x-ray diffraction. The electron diffraction measurements show that after annealing at 660°C the ι-phase (Ce_7O_{12}) is formed at the surface which exhibits a $(\sqrt{7} \times \sqrt{7})$R19.1° structure. Furthermore, a $(\sqrt{27} \times \sqrt{27})$R30° surface structure with a stoichiometry close to Ce_2O_3 is stabilized after annealing at 860°C which can not be attributed to any bulk phase of ceria stable at room temperature. In addition, it is shown that the fully reduced ceria (Ce_2O_3) film exhibits a bixbyite structure. Polycrystalline silicate ($CeSi_xO_y$) and crystalline silicide ($CeSi_{1.67}$) are formed at 850°C and detected at the surface after annealing above 900°C.

¶Electronic mail: joachim.wollschlaeger@uos.de

9 Summary and Outlook

This chapter summarizes the main results of this thesis and gives an outlook addressing future experiments.

In this thesis the structural bulk and surface properties of praseodymia and ceria films grown on Si(111) have been investigated. Furthermore, the thermal stability as well as the possibilities of the preparation of intermediate phases have been explored.

In the first part of this thesis praseodymia films grown on a Si(111) substrate have been investigated. The surface of hexagonal $Pr_2O_3(0001)$ films has been characterized. These films are unstable at ambient conditions due to hydroxide formation. Hence, prior to the surface characterization, the utility of amorphous germanium capping layers has been examined. It has been shown that germanium is a viable choice as capping material since the film integrity is not distorted during transport and after removal of the capping layer. Furthermore, it has been revealed that the hexagonal $Pr_2O_3(0001)$ films are very smooth and do not show mosaic spread as previously reported for cubic $Pr_2O_3(111)$ films [130, 131]. Therefore, it is proposed that the mosaic spread in cubic $Pr_2O_3(111)$ films is formed during the hex $\rightarrow$ cub transition.

Furthermore, the structural changes of stoichiometric $PrO_2(111)$ films grown on Si(111) are correlated with thermally induced oxygen desorption. First of all, grazing incidence x-ray diffraction (GIXRD) measurements reveal that the previously observed lateral pinning to the hex-$Pr_2O_3(0001)$ lattice constant [29] is not breached by the oxygen plasma treatment necessary to obtain stoichiometric $PrO_2(111)$. Furthermore, it was shown that the characteristic desorption peaks are directly linked to the formation of different oxide phases. However, the stabilization of a single intermediate phase (Pr_5O_9) has only been achieved for the strongest desorption signal α' at $\approx$ 650 K. The formation of the Pr_5O_9 phase is accompanied by major structural changes since the lateral pinning is breached during this process. For every other TPD peak two lateral coexisting oxide species with different vertical layer distances are observed.

In the second part the thermal stability of $CeO_2(111)$ films grown on a hex-$Pr_2O_3(0001)$/Si(111) system has been investigated. Several surface structures with long ranged ordered oxygen vacancies could be stabilized by post deposition annealing (PDA) treatment. For instance, a $(\sqrt{7} \times \sqrt{7})R19.1°$ and (4×4) electron diffraction pattern have been observed. These pattern can be directly assigned to the bulk terminated (111) surface of the Ce_7O_{12} and cubic Ce_2O_3 phase, respectively. In contrast, a $(\sqrt{27} \times \sqrt{27})R30°$ surface structure with a stoichiometry close to Ce_2O_3 has been detected which can not be linked to any known ceria phase. It was further revealed that the bulk exhibits different reduction properties than the surface. The x-ray diffraction (XRD) measurements have shown that not the entire film is reduced homogeneously since CeO_2 was still detected at high PDA temperatures. After the praseodymia buffer layer dissolves, a higher oxide phase is formed in the bulk which is not visible at the surface. In addition, the thermal stability of the ceria films is limited due to the formation of crystalline silicide and polycrystalline silicate at elevated temperatures.

The successful preparation of the hex-$Pr_2O_3(0001)$ surface presented here enables in-situ surface studies, for instance, to clarify the origins of the mosaic spread in cub-$Pr_2O_3(111)$

films. It is assumed that the mosaics are formed during the hex $\rightarrow$ cub transition which now can be elucidated in a proper PDA study.

The in this work presented TPD/XRD study gives the opportunity to study the structural influence on the reactivity and selectivity of different chemical reactions involving praseodymia. The oxygen TPD signal can be used as fingerprint for the underlying structural properties, for instance, in future methanol conversion studies.

Another challenging task is the identification of the $(\sqrt{27} \times \sqrt{27})R30°$ surface structure of the ceria films. Up to now, it is unclear whether this structure is the bulk termination of an unknown ceria phase or a surface reconstruction. Direct imaging techniques like atomic force microscopy or scanning tunneling microscopy as well as theoretical calculations would be useful to answer this question.

The presented studies of the $CeO_2(111)$ films have shown that the reduced films are not single phased. Therefore, the question arises if the preparation of single phased intermediate phases is possible. This question could be answered with an additional PDA study using longer annealing times.

In addition, room temperature ferromagnetism was recently discovered for reduced ceria films [153, 162–166]. However, a detailed study correlating the different intermediate phases with the magnetic properties is not available at present. Here, well defined film systems as prepared in this study can be used to elucidate the magnetic properties.

A   Derivations for the spot profile analysis

In this section a simplified expression of the lattice factor $G(\boldsymbol{K})$ for a rough surface with random distributed steps is derived based on the work in Ref. [59]. In the following the abbreviations

$$\beta_S = \beta_S(\boldsymbol{K}_\perp) = \left\langle e^{i\boldsymbol{K}_\perp dh_j} \right\rangle_y = \sum_{h=-\infty}^{\infty} P_h(h)\, e^{i\boldsymbol{K}_\perp dh} \quad \text{and} \tag{A.1}$$

$$\beta_T = \beta_T(\boldsymbol{K}_\parallel) = \left\langle e^{i\boldsymbol{K}_\parallel a\Gamma_y} \right\rangle_y = \sum_{\Gamma=1}^{\infty} P_\Gamma(\Gamma)\, e^{i\boldsymbol{K}_\parallel a\Gamma} \tag{A.2}$$

are used for the Fourier transformation of the terrace width and step height distribution denoted by $P_h(h)$ and $P_\Gamma(\Gamma)$, respectively. As shown in Sec. 2.3.2 the lattice factor for a stepped surface is given by

$$G(\boldsymbol{K}) = \sum_{x=-\infty}^{\infty} \left\langle S_{x+y}(\boldsymbol{K}) S_y^*(\boldsymbol{K})\, e^{i\boldsymbol{K}_\parallel a \sum_{j=y}^{x+y-1} \Gamma_j}\, e^{i\boldsymbol{K}_\perp d \sum_{j=y+1}^{x+y} h_j} \right\rangle_y. \tag{A.3}$$

Here, S_y denote the structural amplitude for geometric distributed terraces (cf. Eq. (2.51)). The terrace widths and step heights are integer multiple Γ_j and h_j of the lateral and vertical lattice constant a and d, respectively. The brackets $\langle ... \rangle_y$ denote averaging with respect to y. By assuming that adjacent steps are uncorrelated, the step height distribution can be considered independent from the terrace width distribution. Thus, Eq. (A.3) can be rewritten as

$$G(\boldsymbol{K}) = \sum_{x=-\infty}^{\infty} \left\langle S_{x+y}(\boldsymbol{K}) S_y^*(\boldsymbol{K})\, e^{i\boldsymbol{K}_\parallel a \sum_{j=y}^{x+y-1} \Gamma_j}\, e^{i\boldsymbol{K}_\perp d \sum_{j=y+1}^{x+y} h_j} \right\rangle_y \tag{A.4}$$

$$= \sum_{x=-\infty}^{\infty} \left\langle S_{x+y}(\boldsymbol{K}) S_y^*(\boldsymbol{K})\, e^{i\boldsymbol{K}_\parallel a \sum_{j=y}^{x+y-1} \Gamma_j} \right\rangle_y \left\langle e^{i\boldsymbol{K}_\perp d \sum_{j=y+1}^{x+y} h_j} \right\rangle_y \tag{A.5}$$

$$= \sum_{x=-\infty}^{\infty} \left\langle S_{x+y}(\boldsymbol{K}) S_y^*(\boldsymbol{K})\, e^{i\boldsymbol{K}_\parallel a \sum_{j=y}^{x+y-1} \Gamma_j} \right\rangle_y \prod_{j=y+1}^{x+y} \left\langle e^{i\boldsymbol{K}_\perp dh_j} \right\rangle_y \tag{A.6}$$

Appendix

In the following the sum over x is evaluated for $x = 0$, $x > 0$ and $x < 0$. The simplest case $x = 0$ results in

$$G_{x=0}(\boldsymbol{K}) = \left\langle S_y(\boldsymbol{K}) S_y^*(\boldsymbol{K}) \right\rangle_y \beta_S^0 \tag{A.7}$$

$$= \left\langle \frac{(1 - e^{i\boldsymbol{K}_{\|}a\Gamma_x})(1 - e^{-i\boldsymbol{K}_{\|}a\Gamma_x})}{(1 - e^{i\boldsymbol{K}_{\|}a})(1 - e^{-i\boldsymbol{K}_{\|}a})} \right\rangle_y \tag{A.8}$$

$$= \frac{2 - \left\langle e^{i\boldsymbol{K}_{\|}a\Gamma_y} \right\rangle_y - \left\langle e^{-i\boldsymbol{K}_{\|}a\Gamma_y} \right\rangle_y}{2(1 - \cos(a\boldsymbol{K}_{\|}))} \tag{A.9}$$

$$= \frac{2 - \beta_T - \beta_T^*}{2(1 - \cos(a\boldsymbol{K}_{\|}))} . \tag{A.10}$$

For $x > 0$ the lattice factor is given by

$$G_{x>0}(\boldsymbol{K}) = \sum_{x>0}^{X} \left\langle S_y(\boldsymbol{K}) S_y^*(\boldsymbol{K}) \, e^{i\boldsymbol{K}_{\|}a \sum_{j=y}^{x+y-1} \Gamma_j} \right\rangle_y \beta_S^x \tag{A.11}$$

$$= \sum_{x>0}^{X} \left\langle \frac{(1 - e^{i\boldsymbol{K}_{\|}a\Gamma_{x+y}})(1 - e^{-i\boldsymbol{K}_{\|}a\Gamma_y})}{2(1 - \cos(a\boldsymbol{K}_{\|}))} \, e^{i\boldsymbol{K}_{\|}a \sum_{j=y}^{x+y-1} \Gamma_j} \right\rangle_y \beta_S^x \tag{A.12}$$

$$= \sum_{x>0}^{X} \left\langle \frac{e^{i\boldsymbol{K}_{\|}a \sum_{j=y}^{x+y-1} \Gamma_j} - e^{i\boldsymbol{K}_{\|}a \sum_{j=y}^{x+y} \Gamma_j} - e^{i\boldsymbol{K}_{\|}a \sum_{j=y+1}^{x+y-1} \Gamma_j} + e^{i\boldsymbol{K}_{\|}a \sum_{j=y+1}^{x+y} \Gamma_j}}{2(1 - \cos(a\boldsymbol{K}_{\|}))} \right\rangle_y \beta_S^x . \tag{A.13}$$

Assuming adjacent terraces Γ_j are uncorrelated, the equation can be further simplified to

$$G_{x>0}(\boldsymbol{K}) = \frac{1}{2(1 - \cos(a\boldsymbol{K}_{\|}))} \sum_{x>0}^{X} \left[\prod_{j=y}^{x+y-1} \left\langle e^{i\boldsymbol{K}_{\|}a\Gamma_j} \right\rangle_y - \prod_{j=y}^{x+y} \left\langle e^{i\boldsymbol{K}_{\|}a\Gamma_j} \right\rangle_y \right. \tag{A.14}$$

$$\left. - \prod_{j=y+1}^{x+y-1} \left\langle e^{i\boldsymbol{K}_{\|}a\Gamma_j} \right\rangle_y + \prod_{j=y+1}^{x+y} \left\langle e^{i\boldsymbol{K}_{\|}a\Gamma_j} \right\rangle_y \right] \beta_S^x$$

$$= \sum_{x>0}^{X} \frac{(\beta_T^x - \beta_T^{x+1} - \beta_T^{x-1} + \beta_T^x)}{2(1 - \cos(a\boldsymbol{K}_{\|}))} \beta_S^x \tag{A.15}$$

$$= \frac{(2 - \beta_T - \frac{1}{\beta_T})}{2(1 - \cos(a\boldsymbol{K}_{\|}))} \sum_{x>0}^{X} (\beta_S \beta_T)^x \tag{A.16}$$

$$= \frac{(2 - \beta_T - \frac{1}{\beta_T})}{2(1 - \cos(a\boldsymbol{K}_{\|}))} \frac{\beta_S \beta_T}{1 - \beta_S \beta_T} . \tag{A.17}$$

The calculations for $x < 0$ are similar to the case $x > 0$ using the complex conjugate values resulting in

$$G_{x<0}(\boldsymbol{K}) = \frac{(2 - \beta_T^* - \frac{1}{\beta_T^*})}{2(1 - \cos(a\boldsymbol{K}_{\|}))} \frac{\beta_S^* \beta_T^*}{1 - \beta_S^* \beta_T^*} . \tag{A.18}$$

Combining Eq. (A.10), Eq. (A.13) and Eq. (A.18) the expression can be simplified to

$$G(\boldsymbol{K}) = G_{x=0}(\boldsymbol{K}) + G_{x>0}(\boldsymbol{K}) + G_{x<0}(\boldsymbol{K}) \tag{A.19}$$

$$= \frac{2 - \beta_T - \beta_T^*}{2(1 - \cos(a\boldsymbol{K}_{\parallel}))} + \frac{(2 - \beta_T - \frac{1}{\beta_T^*})}{2(1 - \cos(a\boldsymbol{K}_{\parallel}))} \frac{\beta_S \beta_T}{1 - \beta_S \beta_T} \tag{A.20}$$

$$+ \frac{(2 - \beta_T^* - \frac{1}{\beta_T^*})}{2(1 - \cos(a\boldsymbol{K}_{\parallel}))} \frac{\beta_S^* \beta_T^*}{1 - \beta_S^* \beta_T^*}$$

$$= \frac{1 - \beta_T}{2(1 - \cos(a\boldsymbol{K}_{\parallel}))} + \frac{(2 - \beta_T - \frac{1}{\beta_T})}{2(1 - \cos(a\boldsymbol{K}_{\parallel}))} \frac{\beta_S \beta_T}{1 - \beta_S \beta_T} + c.c. \tag{A.21}$$

$$= \frac{1 - \beta_T \beta_S - \beta_T + \beta_S \beta_T^2 + 2\beta_S \beta_T - \beta_S \beta_T^2 - \beta_S}{2(1 - \cos(a\boldsymbol{K}_{\parallel}))(1 - \beta_S \beta_T)} + c.c. \tag{A.22}$$

$$= \frac{1 - \beta_T + \beta_T \beta_S - \beta_S}{2(1 - \cos(a\boldsymbol{K}_{\parallel}))(1 - \beta_S \beta_T)} + c.c. \tag{A.23}$$

$$= \frac{(1 - \beta_T)(1 - \beta_S)}{2(1 - \cos(a\boldsymbol{K}_{\parallel}))(1 - \beta_S \beta_T)} + c.c. \ . \tag{A.24}$$

B   List of publications

Peer-reviewed publications

- T. Kuschel, H. Bardenhagen, H. Wilkens, R. Schubert, J. Hamrle, J. Pištora and J. Wollschläger.
  Vectorial magnetometry using magnetooptic Kerr effect including first- and second-order contributions for thin ferromagnetic films.
  J. Phys. D: Appl. Phys., 44:265003, 2011.
  doi:10.1088/0022-3727/44/26/265003

- M. H. Zoellner, J. Dabrowski, P. Zaumseil, A. Giussani, M. A. Schubert, G. Lupina, H. Wilkens, J. Wollschläger, M. Reichling, M. Bäumer and T. Schroeder.
  Stacking behavior of twin-free type-B oriented $CeO_2(111)$ films on hexagonal $Pr_2O_3(0001)/Si(111)$ systems.
  Phys. Rev. B., 85:035302, 2012.
  doi:10.1103/PhysRevB.85.035302

- M. H. Zoellner, P. Zaumseil, H. Wilkens, S. Gevers, J. Wollschläger, Y.-H. Xie, G. Niu and T. Schroeder.
  Stoichiometry-structure correlation of epitaxial $Ce_{1-x}Pr_xO_{2-\delta}$ (x = 0 - 1) thin films on Si(111).
  J. Cryst. Growth, 355:159, 2012.
  doi:10.1016/j.jcrysgro.2012.06.050

- H. Wilkens, O. Schuckmann, R. Oelke, S. Gevers, A. Schaefer, M. Bäumer, M. H. Zoellner, T. Schroeder and J. Wollschläger.
  Stabilization of the ceria ι-phase (Ce_7O_{12}) surface on Si(111).
  Appl. Phys. Lett., 102:111602, 2013.
  doi:10.1063/1.4795867

- H. Wilkens, J. Rodewald, S. Gevers, M. H. Zoellner, T. Schroeder and J. Wollschläger.
  Surface morphology of ultrathin hex-Pr_2O_3 films on Si(111).
  J. Phys. D: Appl. Phys., 46:285306, 2013.
  doi:10.1088/0022-3727/46/28/285306

- H. Wilkens, O. Schuckmann, R. Oelke, S. Gevers, M. Reichling, A. Schaefer, M. Bäumer, M. H. Zoellner, G. Niu, T. Schroeder and J. Wollschläger.
  Structural transitions of epitaxial ceria films on Si(111).
  Phys. Chem. Chem. Phys., 15:18589, 2013.
  doi:10.1039/C3CP52688G

- H. Wilkens, S. Gevers, S. Röhe, A. Schaefer, M. Bäumer, M. H. Zoellner, G. Niu, T. Schroeder and J. Wollschläger.
  Structural Changes of Ultrathin Cub-$PrO_2(111)/Si(111)$ Films Due to Thermally Induced Oxygen Desorption

J. Phys. Chem. C 118:3056, 2014.
doi:10.1088/0022-3727/46/28/285306

- R. Olbrich, H. H. Pieper, R. Oelke, H. Wilkens, J. Wollschläger, M. H. Zoellner, T. Schroeder, and M. Reichling
A well-structured metastable ceria surface
Appl. Phys. Lett. 104:081910, 2014.
doi:10.1063/1.4866667

Non reviewed publications

- M. Suendorf, T. Kuschel, S. Gevers, D. Bruns, A. Knobeler, H. Wilkens, F. Bertram and J. Wollschläger.
XRR and XRD studies on thin Fe-films on MgO(001).
HASYLAB Annual Report (2009)

- C. Otte, M. Suendorf, T. Kuschel, S. Gevers, D. Bruns, H. Wilkens, F. Bertram and J. Wollschläger.
XRR and XRD studies on thin Fe-films on MgO(001).
HASYLAB Annual Report (2010)

- H. Wilkens, M. H. Zoellner, T. Schroeder and J. Wollschläger.
Investigation of the stacking behavior of $CeO_2(111)$ films on hexagonal-$Pr_2O_3(0001)/Si(111)$ systems.
HASYLAB Annual Report (2010)

- S. Gevers, A. Knobeler, D. Bruns, N. Jeppesen, H. Wilkens and J. Wollschläger.
Epitaxy of cubic Pr_2O_3 on boron passivated Si(111).
HASYLAB Annual Report (2010)

- H. Wilkens, J. Rodewald, S. Gevers, M. H. Zoellner, T. Schroeder and J. Wollschläger.
Investigation of the thermal stability of a-Ge on hex-Pr_2O_3/Si(111).
HASYLAB Annual Report (2011)

- H. Wilkens, S. Gevers, M. H. Zoellner, T. Schroeder and J. Wollschläger.
In-situ XRD investigations of the oxidation process in ultra thin praseodymia films on Si(111).
HASYLAB Annual Report (2011)

- S. Gevers, H. Wilkens, H. H. Pieper, M. Reichling and J. Wollschläger.
Annealed CeO_2/hex-Pr_2O_3/Si(111) multilayer systems.
HASYLAB Annual Report (2011)

- H. Wilkens, O. Schuckmann, M. H. Zoellner, T. Schroeder and J. Wollschläger.
Structural transitions of epitaxial ceria films on Si(111).
HASYLAB Annual Report (2012)

- H. Wilkens, S. Röhe, A. Schaefer, M. Bäumer, M. H. Zoellner, T. Schroeder and J. Wollschläger.
  Structural changes of plasma treated ultra thin cub-PrO_2(111)/Si(111) films during oxygen desorption.
  HASYLAB Annual Report (2012)

- H. Wilkens, S. Gevers, M. H. Zoellner, T. Schroeder and J. Wollschläger.
  In-situ XRD investigations of the oxidation process of ultra thin Pr_2O_3(111) films on Si(111).
  HASYLAB Annual Report (2012)

Bibliography

[1] D. Xue, K. Betzler, and H. Hesse. Dielectric constants of binary rare-earth compounds. *J. Phys.: Condens. Matter*, 12:3113, 2000.

[2] R. D. Shannon, M. A. Subramanian, T. H. Allik, H. Kimura, M. R. Kokta, M. H. Randles, and G. R. Rossman. Dielectric constants of yttrium and rareearth garnets, the polarizability of gallium oxide, and the oxide additivity rule. *J. Appl. Phys.*, 67:3798, 1990.

[3] G. V. Antoshin, K. M. Minachev, and D. R. Dmitriev. Mobility of oxygen and catalytic properties of rare earth oxides with respect to oxidation of hydrogen. *Russ. Chem. Bull.*, 16:1793, 1967.

[4] J. Kwo, M. Hong, B. Busch, D. A. Muller, Y. J. Chabal, A. R. Kortan, J. P. Mannaerts, B. Yang, P. Ye, H. Gossmann, A. M. Sergent, K. K. Ng, J. Bude, W. H. Schulte, E. Garfunkel, and T. Gustafsson. Advances in high k gate dielectrics for Si and III-V semiconductors. *J. Cryst. Growth*, 251:645, 2003.

[5] S.-Y. Zheng, , A. M. Andersson-Fäldt, B. Stjerna, and C. G. Granqvist. Optical properties of sputter-deposited cerium oxyfluoride thin films. *Appl. Opt.*, 32:6303, 1993.

[6] T. Marcinow and K. Truszkowska. Rare earth oxide films: their preparation and optical properties. *Appl. Opt.*, 20:1755, 1981.

[7] G. A. M. Hussein. Rare earth metal oxides: formation, characterization and catalytic activity Thermoanalytical and applied pyrolysis review. *J. Anal. Appl. Pyrolysis*, 37:111, 1996.

[8] G. E. Moore. Cramming more components onto integrated circuits. *Electronics*, 38, 1965.

[9] G. D. Wilk, R. M. Wallace, and J. M. Anthony. High-k gate dielectrics: Current status and materials properties considerations. *J. Appl. Phys.*, 89:5243, 2001.

[10] D. G. Schlom, S. Guha, and S. Datta. Gate Oxides Beyond SiO$_2$. *MRS Bulletin*, 33:1017, 2008.

[11] J. Robertson. High dielectric constant oxides. *Eur. Phys. J. Appl. Phys.*, 28:265, 2004.

[12] A. G. Frangoul, K. B. Sundaram, and P. F. Wahid. The fabrication of metal-oxide-semiconductor transistors using cerium dioxide as a gate oxide material. *J. Vac. Sci. Technol. B*, 9:181, 1991.

[13] T. Schroeder, T.-L. Lee, L. Libralesso, I. Joumard, J. Zegenhagen, P. Zaumseil, C. Wenger, G. Lupina, G. Lippert, J. Dabrowski, and H.-J. Müssig. Structure and strain relaxation mechanisms of ultrathin epitaxial Pr$_2$O$_3$ films on Si(111). *J. Appl. Phys.*, 97:074906, 2005.

[14] T. Schroeder, P. Zaumseil, G. Weidner, G. Lupina, Ch. Wenger, and H.-J. Müssig. Structure, twinning behavior, and interface composition of epitaxial Si(111) films on hex-Pr$_2$O$_3$(0001)/Si(111) support systems. *J. Appl. Phys.*, 98:123513, 2005.

[15] T. Schroeder, P. Zaumseil, G. Weidner, Ch. Wenger, J. Dabrowski, and H.-J. Müssig. On the epitaxy of twin-free cubic (111) praseodymium sesquioxide films on Si(111). *J. Appl. Phys.*, 99:014101, 2006.

[16] J. P. Liu, P. Zaumseil, E. Bugiel, and H. J. Osten. Epitaxial growth of Pr$_2$O$_3$ on Si(111) and the observation of a hexagonal to cubic phase transition during postgrowth N$_2$ annealing. *Appl. Phys. Lett.*, 79:671, 2001.

[17] K. Otsuka, K. Jinno, and A. Morikawa. Active and selective catalysts for the synthesis of C$_2$H$_4$ and C$_2$H$_6$ via oxidative coupling of methane. *J. Catal.*, 100:353, 1986.

[18] K. Otsuka, Y. Wang, E. Sunada, and I. Yamanaka. Direct Partial Oxidation of Methane to Synthesis Gas by Cerium Oxide. *J. Catal.*, 175:152, 1998.

[19] M.P. Rosynek. Catalytic Properties of Rare Earth Oxides. *Catal. Rev. -Sci. and Eng.*, 16:111, 1977.

[20] A. Trovarelli. Catalytic Properties of Ceria and CeO$_2$-Containing Materials. *Catal. Rev. - Sci. Eng.*, 38:439, 1996.

[21] J. Guzman, S. Carrettin, J. C. Fierro-Gonzalez, Y. Hao, B. C. Gates, and A. Corma. CO Oxidation Catalyzed by Supported Gold: Cooperation between Gold and Nanocrystalline Rare-Earth Supports Forms Reactive Surface Superoxide and Peroxide species. *Angew. Chem., Int. Ed.*, 44:4778, 2005.

[22] V.R. Choudhary, B.S. Uphade, and A.S. Mamman. Large enhancement in methane-to-syngas conversion activity of supported ni catalysts due to precoating of catalyst ssupport with MgO, CaO or rare earth oxide. *Catalysis Letters*, 32:387, 1995.

[23] G. Adachi and N. Imanaka. The Binary Rare Earth Oxides. *Chem. Rev.*, 98:1479, 1998.

[24] T. Campbell. Ultrathin metal films and particles on oxide surfaces: structural, electronic and chemisorptive properties. *Surf. Sci. Rep.*, 27:1, 1997.

[25] R. Henry. Surface studies of supported model catalysts. *Surf. Sci. Rep.*, 31:231, 1998.

[26] M. Bäumer and H.-J. Freund. Metal deposits on well-ordered oxide films. *Prog. Surf. Sci.*, 61:127, 1999.

[27] P. Sonström, J. Birkenstock, Y. Borchert, L. Schilinsky, P. Behrend, K. Gries, K. Müller, A. Rosenauer, and M. Bäumer. Nanostructured praseodymium oxide: Correlation between phase transitions and catalytic activity. *ChemCatChem*, 2:694, 2010.

[28] O. Seifarth, Ch. Walczyk, G. Lupina, J. Dabrowski, P. Zaumseil, G. Weidner, H.-J. Müssig, and T. Schroeder. Dielectric properties of single crystalline $PrO_2(111)$ / $Si(111)$ heterostructures: Amorphous interface and electrical instabilities. *J. Appl. Phys.*, 106:104105, 2009.

[29] T. Weisemoeller, F. Bertram, S. Gevers, A. Greuling, C. Deiter, H. Tobergte, M. Neumann, A. Giussani, T. Schroeder, and J. Wollschläger. Post deposition annealing induced transition from hexagonal Pr_2O_3 to cubic PrO_2 films on $Si(111)$. *J. Appl. Phys.*, 105:124108, 2009.

[30] E. J. Preisler, O. J. Marsh, R. A. Beach, and T. C. McGill. Stability of cerium oxide on silicon studied by x-ray photoelectron spectroscopy. *J. Vac. Sci. Technol. B*, 19:1611, 2001.

[31] C. Kittel. *Einführung in die Festkörperphysik*. Oldenbourg Wissenschaftsverlag, 2006.

[32] K. Kopitzki and P. Herzog. *Einführung in die Festkörperphysik, 5. ed.* Teubner, 2004.

[33] K. Oura, V. Lifshits, A. Saranin, and M. Katayama. *Surface Science*. Springer, 2003.

[34] A. Bravais. Mémoire sur les systèmes formés par les points distribués régulièrement sur un plan ou dans l'espace. *J. Ecole Polytech.*, 19:1, 1850.

[35] W. H. Miller. *A Treatise on Crystallography*. Cambridge, 1839.

[36] R. Park and H. H. Madden. Annealing changes on the (100) surface of palladium and their effect on CO adsorption. *Surf. Sci.*, 11:188, 1968.

[37] E. A. Wood. Vocabulary of surface crystallography. *J. Appl. Phys.*, 35:1306, 1964.

[38] S. Hashimoto, J. L. Peng, W. M. Gibson, L. J. Schowalter, and R. W. Fathauer. Strain measurement of epitaxial CaF_2 on $Si(111)$ by MeV ion channeling. *Appl. Phys. Lett.*, 47:1071, 1985.

[39] P. M. Marcus. Epitaxial strain and epitaxial bending. *Surf. Sci.*, 366:219, 1996.

[40] T. Hammerschmidt, P. Kratzer, and M. Scheffler. Elastic response of cubic crystals to biaxial strain: Analytic results and comparison to density functional theory for InAs. *Phys. Rev. B*, 75:235328, 2007.

[41] W. H. Bragg and W. L. Bragg. The reflection of X-rays by crystals. *Proc. R. Soc. Lond. A*, 88:428, 1913.

[42] W. Friedrich, P. Knipping, and M. Laue. Interferenz-Erscheinungen bei Röntgenstrahlen. *Die Naturwissenschaften*, 16:361, 1952.

[43] R. Feidenhans'l. Surface structure determination by x-ray diffraction. *Surface Science Reports*, 10:105, 1989.

[44] I. K. Robinson and D. J. Tweet. Surface x-ray diffraction. *Rep. Prog. Phys.*, 55:599, 1992.

[45] C. Deiter. *Röntgenstrukturanalyse von Halbleiter-Isolator-Schichtsystemen*. PhD thesis, Universität Bremen, 2005.

[46] F. Bertram. *The structure of ultrathin iron oxide films studied by x-ray diffraction*. PhD thesis, Universität Osnabrück, 2012.

[47] A. J. C. Wilson and V. Geist. *International tables for X-ray crystallography*. Kluwer Academic Publishers, 1992.

[48] B. Warren. *X-ray Diffraction*. Dover publications Inc., 1990.

[49] B. T. M. Willis and A. W. Pryor. *Thermal vibration in crystallography*. Cambridge University Press, 1975.

[50] M. Ladd and R. Palmer. *Structure determination by x-ray crystallography*. Kluwer Academic Publishers, 2003.

[51] S. Mròz. Physical foundation of quantitative auger analysis. *Prog. Surf. Sci.*, 46:377, 1994.

[52] M.A. Van Hove, W.-H. Weinberg, and C.-M. Chan. *Low-Energy Electron Diffraction*. Springer, 1986.

[53] M. Henzler. Defects at semiconductor surfaces. *Surf. Sci.*, 152:963, 1982.

[54] M. Horn-von Hoegen. Growth of semiconductor layers studied by spot profile analysing low energy electron diffraction. *Z. KRISTALLOGR*, 214:591, 1999.

[55] R. L. Park and J. E. Houston. The effect of registry degeneracy on LEED beam profiles. *Surf. Sci.*, 18:213, 1969.

[56] J. E. Houston and R. L. Park. Low-energy-electron diffraction from imperfect structures. *Surf. Sci.*, 21:209, 1970.

[57] M. Henzler. Atomic Steps on Single Crystals: Experimental Methods and Properties. *Appl. Phys.*, 9:11, 1976.

[58] T.-M. Lu and M. G. Lagally. Diffraction from surfaces with randomly distributed steps. *Surf. Sci.*, 120:47, 1982.

[59] J. Wollschläger. *Ordnungsvorgänge in einatomaren Metallschichten auf hochindizierten Metallflächen.* PhD thesis, Universität Hannover, 1990.

[60] D. Thielking. *Srukturelle Untersuchungen zur Heteroepitaxie: Wachstum ultradünner Silberschichten auf Silizium(111)-7 × 7-Substraten.* PhD thesis, Universität Hannover, 1993.

[61] S. Gevers. *Praseodymia on non-passivated and passivated Si(111) surfaces.* PhD thesis, Universität Osnabrück, 2010.

[62] J. Wollschläger. Diffraction from surfaces with randomly distributed structural defects. *Surf. Sci.*, 328:3, 1995.

[63] P. Auger. Sur l'Effect Photoelectrique Compose. *Le Journal de Physique et le Radium*, 6:205, 1925.

[64] J. C. Vickerman. *Surface Analysis: The Principal Techniques.* Wiley, 1997.

[65] C. C. Chang. Auger electron spectroscopy. *Surf. Sci.*, 25:53, 1971.

[66] P. W. Palmberg, G. E. Riach, R. E. Weber, and N. C. MacDonald. *Handbook of Auger Electron Spectroscopy.* MN: Physical Electronics, 1972.

[67] S. Huefner. *Photoelectron spectroscopy: principles and applications.* Springer, 1995.

[68] H. Hertz. Über den Einfluss des ultravioletten Lichtes auf die elektrische Entladung. *Wiedemannsche Annalen*, 31:983, 1887.

[69] W. Hallwachs. Über den Einfluss des Lichtes auf elektrostatisch geladene Koerper. *Wiedemannsche Annalen*, 33:301, 1888.

[70] A. Einstein. Über einen die Erzeugung und Verwandlung des Lichtes betreffenden heuristichen Gesichtspunkt. *Annalen der Physik*, 17:132, 1905.

[71] B. Zimmermann. *Epitaktisches Wachstum und Charakterisierung ultradünner Eisenoxidschichten auf Magnesiumoxid(001).* PhD thesis, Universität Osnabrück, 2010.

[72] B. Feuerbacher, B. Fitton, and R. F. Willis. *Photoemission and the Electronic Properties of Surfaces.* Wiley, 1978.

[73] H. C. Wolf and H. Haken. *The physics of atoms and quanta.* Spinger, 1994.

[74] S. Hüffner and G. K. Wertheim. Core-Electron Splitting and Hyperfine Fields in Transition-Metal Compounds. *Phys. Rev. B*, 7:2333, 1973.

[75] J. M. Hollas. *High resolution spectroscopy*. Butterworths and Co, 1982.

[76] D. Briggs and J. C. Riviere. *Practical surface analysis by Auger and X-Ray photoelectron spectroscopy*. Wiley, 1983.

[77] U. Gelius. Binding Energies and Chemical Shifts in ESCA. *Physica Scripta*, 9:133, 1974.

[78] D. A. Shirley. High-resolution x-ray photoemission spectrum of the valence band of gold. *Phys. Rev. B*, 5:4709, 1972.

[79] S. Tougaard. Inelastic background correction and quantitative surface analysis. *J. Electron Spectrosc. Relat. Phenom.*, 52:243, 1990.

[80] A. Kotani and H. Ogasawara. Theory of core-level spectroscopy of rare-earth oxides. *J. Electron Spectrosc. Relat. Phenom.*, 60:257, 1992.

[81] O. Schuckmann. Plasmamodifzierung von Praseodym- und Ceroxidschichten. Master's thesis, Universität Osnabrück, 2012.

[82] S. J. Lombardo and A. T. Bell. A review of theoretical models of adsorption, diffusion, desorption, and reaction of gases on metal surfaces. *Surf. Sci. Rep.*, 13:1, 1991.

[83] R.P. Turcotte, J.M. Warmkessel, R.J.D. Tilley, and L. Eyring. On the Phase Interval $PrO_{1.50}$ to $PrO_{1.71}$ in the Praseodymium Oxide-Oxygen System. *J. Solid State Chem.*, 3:265, 1971.

[84] G. Adachi, N. Imanaka, and Z. C. Kang, editors. *Binary Rare Earth Oxides*. Kluwer Academic Publishers, 2005.

[85] S. P. Ray and D. E. Cox. Neutron diffraction determination of the crystal structure of Ce_7O_{12}. *J. Solid State Chem.*, 15:333, 1975.

[86] E.A. Kümmerle and G. Heger. The Structures of $C\text{-}Ce_2O_{3+\delta}$, Ce_7O_{12}, and $Ce_{11}O_{20}$. *J. Solid State Chem.*, 147:485, 1999.

[87] L. Eyring and N.C. Beanziger. On the Structure and Related Properties of the Oxides of Praseodymium. *J. Appl. Phys.*, 33:428, 1962.

[88] A. Schaefer, V. Zielasek, Th. Schmidt, A. Sandell, M. Schowalter, O. Seifarth, L. E. Walle, Ch. Schulz, J. Wollschläger, T. Schroeder, A. Rosenauer, J. Falta, and M. Bäumer. Growth of praseod oxide on Si(111) under oxygen-deficient conditions. *Phys. Rev. B.*, 80:045414, 2009.

[89] S. Gevers, J. I. Flege, B. Kaemena, D. Bruns, T. Weisemoeller, J. Falta, and J. Wollschläger. Improved epitaxy of ultrathin praseodymia films on chlorine passivated Si(111) reducing silicate interface formation. *Appl. Phys. Lett.*, 97:242901, 2010.

[90] T. Weisemoeller, C. Deiter, F. Bertram, S. Gevers, A. Giussani, P. Zaumseil, T. Schroeder, and J. Wollschläger. Epitaxy of Single Crystalline PrO_2 films on Si(111). *Appl. Phys. Lett.*, 93:032905, 2008.

[91] S. Gevers, T. Weisemoeller, D. Bruns, A. Giussani, T. Schroeder, and J. Wollschläger. Post-deposition annealing of praseodymia films on Si(111) at low temperatures. *J. Phys.: Condens. Matter*, 23:115904, 2011.

[92] A. Schaefer, S. Gevers, V. Zielasek, T. Schroeder, J. Falta, J. Wollschläger, and M. Bäumer. Photoemission study of praseodymia in its highest oxidation state: The necessity of in situ plasma treatment. *J. Chem. Phys.*, 134:054701, 2011.

[93] S. Gevers, T. Weisemoeller, A. Schaefer, V. Zielasek, M. Bäumer, and J. Wollschläger. Structure of oxygen plasma-treated ultra-thin praseodymia films on Si(111). *Phys. Rev. B*, 83:193408, 2011.

[94] T. Inoue, Y. Yamamoto, S. Koyama, S. Suzuki, and Y. Ueda. Epitaxial growth of CeO_2 layers on silicon. *Appl. Phys. Lett.*, 56:1332, 1990.

[95] T. Inoue, M. Osonoe, H. Tohda, M. Hiramatsu, Y. Yamamoto, A. Yamanaka, and T. Nakayama. Low-temperature epitaxial growth of cerium dioxide layers on (111) silicon substrates. *J. Appl. Phys.*, 69:8313, 1991.

[96] H. Nagata, M. Yoshimoto, H. Koinuma, E. Min, and N. Haga. Type-B epitaxial growth of CeO_2 thin film on Si(111) substrate. *J. Cryst. Growth*, 123:1, 1992.

[97] T. Chikyow, S. M. Bedair, L. Tye, and N. A. ElMasry. Reaction and regrowth control of CeO_2 on Si(111) surface for the silicon-on-insulator structure. *Appl. Phys. Lett.*, 65:1030, 1994.

[98] J. I. Flege, B. Kaemena, S. Gevers, F. Bertram, T. Wilkens, D. Bruns, J. Bätjer, T. Schmidt, J. Wollschläger, and J. Falta. Silicate-free growth of high-quality ultrathin cerium oxide films on Si(111). *Phys. Rev. B*, 84:235418, 2011.

[99] J. Zarraga-Colina, R. M. Nix, and H. Weiss. A novel approach to the epitaxial growth of CeO_2 films on Si(111). *Surf. Sci.*, 563:L251, 2004.

[100] M. H. Zoellner, J. Dabrowski, P. Zaumseil, A. Giussani, M. A. Schubert, G. Lupina, H. Wilkens, J. Wollschläger, M. Reichling, M. Bäumer, and T. Schroeder. Stacking behavior of twin-free type-B oriented CeO_2(111) films on hexagonal Pr_2O_3(0001)/Si(111) systems. *Phys. Rev. B*, 85:035302, 2012.

[101] T. Weisemoeller. *X-ray analysis of praseodymia*. PhD thesis, Universität Osnabrück, 2009.

[102] J. M. Haschke and L. Eyring. Hydrothermal equilibriums and crystal growth of rare earth oxides, hydroxides, hydroxynitrates, and hydroxycarbonates. *Inorg. Chem.*, 10:2267, 1971.

[103] Z.C. Kang and L. Eyring. The solvolytic disproportionation of mixed-valence compounds: II. $Tb_{11}O_{20}$. *J. Solid State Chem.*, 75:60, 1988.

[104] B. Gehl, U. Leist, V. Aleksandrovic, P. Nickut, V. Zielasek, H. Weller, K. Al-Shamery, and M. Bäumer. Design of a UHV-compatible rf plasma source and its application to self-assembled layers of $CoPt_3$ nanoparticles. *Rev. Sci. Instrum.*, 77:083902, 2006.

[105] S. Mähl. *Grundlegende Untersuchungen zur Charakterisierung plasmamodifizierter Polyolefinoberflächen mittels Röntgen-Photoelektronenspektroskopie.* PhD thesis, Universität Osnabrück, 1997.

[106] K. Wille. *Physik der Teilchenbeschleuniger und Synchrotronstrahlungsquellen.* Teubner, 1996.

[107] J. Falta and T. Möller. *Forschung mit Synchrotornstrahlung.* Teubner, 2010.

[108] O. Seeck, C. Deiter, K. Pflaum, F. Bertram, A. Beerlink, J. Franz, H. Horbach, H. Schulte-Schrepping, B. Murphy, M. Greve, and O. Magnussen. The high-resolution diffraction beamline P08 at PETRA III. *J. Synchrotron Rad.*, 19:30, 2012.

[109] W. Caliebe, U. Brüggmann, M. Lohmann, and P. Machek. New Equipment at W1. Technical report, HASYLAB/DESY, 2007.

[110] S. Gevers. SPA-LEED - Untersuchungen von Praseodymoxidschichten auf Si(111) - substraten. Diploma thesis, Universität Osnabrück, 2007.

[111] A. Knobeler. Praseodymoxidschichten auf Bor-passivierten Si(111)-Oberflächen. Diploma thesis, Universität Osnabrück, 2010.

[112] M. Suendorf. *Investigation of the growth process of thin iron oxide films: Analysis of X-ray Photoemission Spectra by Charge Transfer Multiplet calculations.* PhD thesis, Universität Osnabrück, 2012.

[113] O. Höfert. Herstellung und Charakterisierung von Eisenoxidschichten. Master's thesis, Universität Osnabrück, 2009.

[114] A. Schaefer. *Herstellung und Charakterisierung dünner Praseodymoxid-Schichten auf Silizium-Substraten als Modellsystem für die Katalyse und Mikroelektronik.* PhD thesis, Universität Bremen, 2010.

[115] D. Bruns. *Structure and morphology of ultrathin iron and iron oxide films on Ag(001).* PhD thesis, Universität Osnabrück, 2012.

[116] U. Scheithauer, G. Meyer, and M. Henzler. A new LEED Instrument for Quantitative Spot Profile Analysis. *Surface Sciene*, 178:441, 1986.

[117] N. A. Bojarczuk, M. Copel, S. Guha, V. Narayanan, E. J. Preisler, F. M. Ross, and H. Shang. Epitaxial silicon and germanium on buried insulator heterostructures and devices. *Appl. Phys. Lett.*, 83:5443, 2003.

[118] J.W. Seo, Ch. Dieker, A. Tapponnier, Ch. Marchiori, M. Sousa, J.-P. Locquet, J. Fompeyrine, A. Ispas, C. Rossel, Y. Panayiotatos, A. Sotiropoulos, and A. Dimoulas. Epitaxial germanium-on-insulator grown on (001) Si. *Microelectron. Eng.*, 84:2328, 2007.

[119] H. Tanoto, S. F. Yoon, W. K. Loke, E. A. Fitzgerald, C. Dohrman, B. Narayanan, M. T. Doan, and C. H. Tung. Growth of GaAs on vicinal Ge surface using low-temperature migration-enhanced epitaxy. *J. Vac. Sci. Technol. B*, 24:152, 2006.

[120] Y. Borchert, P. Sonström, M. Wilhelm, H. Borchert, and M. Bäumer. Nanostructured Praseodymium Oxide: Preparation, Structure, and Catalytic Properties. *J. Phys. Chem. C*, 112:3054, 2008.

[121] E. J. Tarsa, J. S. Speck, and McD. Robinson. Pulsed laser deposition of epitaxial silicon/h-Pr_2O_3/silicon heterostructures. *Appl. Phys. Lett.*, 63:539, 1993.

[122] A. Schaefer, T. Schroeder, G. Lupina, Y. Borchert, J. Dabrowski, Ch. Wenger, and M. Bäumer. Heteroepitaxial praseodymium sesquioxide films on Si(111): A new model catalyst system for praseodymium oxide based catalysts. *Surf. Sci.*, 601:1473, 2007.

[123] N. M. Jeutter, W. Moritz, A. Sidorenko, and A. Stierle. Crystalline Pr_2O_3 monolayers on Si(111). *Appl. Phys. Lett.*, 90:062906, 2007.

[124] L. Libralesso, T. Schroeder, T.-L. Lee, and J. Zegenhagen. Initial stages of the epitaxial growth of Pr_2O_3 on Si(111) studied by LEED and STM. *Surf. Sci.*, 598:L347, 2005.

[125] I. Khidirov and V. T. Om. Localization of hydrogen atoms in rare earth metal trihydroxides $R(OH)_3$. *Phys. Status Solidi A*, 140:59, 1993.

[126] O. Greis, R. Ziel, B. Breidenstein, A. Haase, and T. Petzel. The crystal structure of the low-temperature A-type modification of Pr_2O_3 from X-ray powder and electron single crystal diffraction. *J. Alloys Compd.*, 216:255, 1994.

[127] J. Wollschläger, J. Falta, and M. Henzler. Electron diffraction at stepped homogeneous and inhomogeneous surfaces. *Appl. Phys. A*, 50:57, 1990.

[128] D. A. Hansen and J. B. Hudson. The adsorption kinetics of molecular oxygen and the desorption kinetics of GeO on Ge(100). *Surf. Sci.*, 292:17, 1993.

[129] S. K. Wang, K. Kita, C. H. Lee, T. Tabata, T. Nishimura, K. Nagashio, and A. Toriumi. Desorption kinetics of GeO from GeO_2/Ge structure. *J. Appl. Phys.*, 108:054104, 2010.

[130] S. Gevers, T. Weisemoeller, B. Zimmermann, F. Bertram, C. Deiter, and J. Wollschläger. Structural phase transition of ultra thin PrO_2 films on Si(111). *J. Phys.: Condens. Matter*, 21:175408, 2009.

[131] S. Gevers, T. Weisemoeller, B. Zimmermann, C. Deiter, and J. Wollschläger. Structure and stability of cub-Pr_2O_3 films on Si(111) under post deposition annealing conditions. *Phys. Status Solidi C*, 7:292, 2010.

[132] S.K. Bhaskaran and V.T. Bhat. Catalytic activity of CeO_2 and Pr_2O_3 for the liquid-phase benzylation of *o* - xylene to 3,4 - dimethyldiphenylmethane. *React. Kinet. Catal. Lett.*, 75:239, 2002.

[133] R. D. Köhn, Z. Pan, J. Sun, and C. Liang. Ring-Opening Polymerization of D,L-Lactide with Bis(trimethyl triazacyclohexane)Praseodymium Triflate. *Catal. Commun.*, 4:33, 2003.

[134] S.W. Bedell, A. Reznicek, K. Fogel, J. Ott, and D.K. Sadana. Strain and lattice engineering for Ge FET devices. *Mater. Sci. Semicond. Process.*, 9:423, 2006.

[135] O. Seifarth, B. Dietrich, P. Zaumseil, A. Giussani, P. Storck, and T. Schroeder. Integration of strained and relaxed silicon thin films on silicon wafers via engineered oxide heterostructures: Experiment and theory. *J. Appl. Phys.*, 108:073526, 2010.

[136] A. Giussani, P. Rodenbach, P. Zaumseil, J. Dabrowski, R. Kurps, G. Weidner, H.-J. Müssig, P. Storck, J. Wollschläger, and T. Schroeder. Atomically smooth and single crystalline $Ge(111)/cubic-Pr_2O_3(111)/Si(111)$ heterostructures: Structural and chemical composition study. *J. Appl. Phys.*, 105:033512, 2009.

[137] G. Saint-Girons, P. Regreny, L. Largeau, G. Patriarche, and G. Hollinger. Monolithic integration of InP based heterostructures on silicon using crystalline Gd_2O_3 buffers. *Appl. Phys. Lett.*, 91:241912, 2007.

[138] L. Tarnawska, A. Giussani, P. Zaumseil, M. Schubert, R. Paszkiewicz, O. Brandt, P. Storck, and T. Schroeder. Single crystalline Sc_2O_3/Y_2O_3 heterostructures as novel engineered buffer approach for GaN ingregration on Si(111). *J. Appl. Phys.*, 108:063502, 2010.

[139] A. F. Diwell, R. R. Rajaram, H. A. Shaw, and T. J. Treux. *The role of ceria in three-way catalysts, in Catalysis Automotive Pollution Control, Vol. 71.* Elsevier, 1991.

[140] Y. Takasu, M. Matsui, and Y. Matsuda. The catalytic contribution of the lattice oxygen atoms of praseodymium oxide to the oxidation of carbon monoxide. *J. Catal.*, 76:61, 1982.

[141] K. Asami, K.-i. Kusakabe, N. Ashi, and Y. Ohtsuka. Synthesis of ethane and ethylene from methane and carbon dioxide over praseodymium oxide catalysts. *Appl. Catal. A*, 156:43, 1997.

[142] E. M. Kennedy and N. W. Cant. Comparison of the oxidative dehydrogenation of ethane and oxidative coupling of methane over rare earth oxides. *Appl. Catal.*, 75:321, 1991.

[143] B. G. Hyde, D. J. M. Bevan, and L. Eyring. On the Praseodymium+Oxygen System. *Philos. Trans. R. Soc. London. Ser. A*, 259:583, 1966.

[144] G. Zhou and J. Grote. Thermodynamic Investigation of the Redox Properties for Ceria-Hafnia, Ceria-Terbia, and Ceria-Praseodymia Solid Solutions. *J. Phys. Chem. B*, 112:9869, 2008.

[145] Y. Takasu, M. Matsui, H. Tamura, S. Kawamura, Y. Matsuda, and I. To-joshima. Temperature-Programmed Desorption on the Unstable Lattice Oxygen of Praseodymium Oxide. *J. Catal.*, 69:51, 1981.

[146] P. Zaumseil and T. Schroeder. About the strain state of different metal oxide layers epitaxially grown on Si(111). *J. Phys. D: Appl. Phys.*, 44:055403, 2011.

[147] R. G. Haire and L. Eyring. *Handbook on the Physics and Chemistry of Rare Earths, Vol 18.* Elsevier, 1994.

[148] Hei Wong, B. L. Yang, Shurong Dong, H. Iwai, K. Kakushima, and P. Ahmet. Current conduction and stability of CeO_2/La_2O_3 stacked gate dielectric. *Appl. Phys. Lett.*, 101:233507, 2012.

[149] E. Miranda, S. Kano, C. Dou, K. Kakushima, J. Suñè, and H. Iwai. Nonlinear conductance quantization effects in CeO_x/SiO_2-based resistive switching devices. *Appl. Phys. Lett.*, 101:012910, 2012.

[150] K. Mohan Kant, V. Esposito, and N. Pryds. Strain induced ionic conductivity enhancement in epitaxial $Ce_{0.9}Gd_{0.1}O_{2-\delta}$ thin films. *Appl. Phys. Lett.*, 100:033105, 2012.

[151] Zhi-Peng Li, T. Mori, G. J. Auchterlonie, Jin Zou, and J. Drennan. Direct evidence of dopant segregation in Gd-doped ceria. *Appl. Phys. Lett.*, 98:093104, 2011.

[152] V. F. Solovyov, M. Gibert, T. Puig, and X. Obradors. Size-dependent strain in epitaxial (001) gadolinium-doped ceria nanoislands. *Appl. Phys. Lett.*, 97:172503, 2010.

[153] R. K. Singhal, P. Kumari, A. Samariya, Sudhish Kumar, S. C. Sharma, Y. T. Xing, and E. B. Saitovitch. Role of electronic structure and oxygen defects in driving ferromagnetism in nondoped bulk CeO_2. *Appl. Phys. Lett.*, 97:172503, 2010.

[154] P.R. Subramanian. *Ce-O (cerium-oxygen), Binary Alloy Phase Diagrams, 2nd ed.* ASM International, 1990.

[155] D. J. M. Bevan. Ordered intermediate phases in the system CeO_2-Ce_2O_3. *J . Inorg. Nucl. Chem.*, 1:49, 1955.

[156] J. P. Holgado, R. Alvarez, and G. Munuera. Study of CeO_2 XPS spectra by factor analysis: reduction of CeO_2. *Appl. Surf. Sci.*, 161:301, 2000.

[157] F. Esch, S. Fabris, L. Zhou, T. Montini, C. Africh, P. Fornasiero, G. Comelli, and R. Roseil. Electron Localization Determines Defect Formation on Ceria Substrates. *Science*, 309:752, 2005.

[158] M.L. Trudeau, A. Tschope, and J.Y. Ying. XPS investigation of surface oxidation and reduction in nanocrystalline $Ce_xLa_{1-x}O_{2-y}$. *Surf. Interface Anal.*, 23:219, 1995.

[159] G. A. Deluga, J. R. Salge, L. D. Schmidt, and X. E. Verykios. Renewable Hydrogen from Ethanol by Autothermal Reforming. *Science*, 303:993, 2004.

[160] S. Torbrügge, M. Reichling, A. Ishiyama, S. Morita, and O. Custance. Evidence of Sub-surface Oxygen Vacancy Ordering on Reduced CeO$_2$(111). *Phys. Rev. Lett.*, 99:056101, 2007.

[161] H. H. Pieper, C. Derks, M. H. Zoellner, R. Olbrich, L. Tröger, T. Schroeder, M. Neu-mann, and M. Reichling. Morphology and nanostructure of CeO$_2$(111) surfaces of single crystals and Si(111) supported ceria films. *Phys. Chem. Chem. Phys.*, 14:15361, 2012.

[162] R. K. Singhal, P. Kumari, S. Kumar, S. N. Dolia, Y. T. Xing, M. Alzamora, U. P. Deshpande, T. Shripathi, and E. Saitovitch. Room temperature ferromagnetism in pure and Co- and Fe-doped CeO$_2$ dilute magnetic oxide: effect of oxygen vacancies and cation valence. *J. Phys. D: Appl. Phys.*, 44:165002, 2011.

[163] M. Chandra Dimri, H. Khanduri, H. Kooskora, J. Subbi, I. Heinmaa, A. Mere, J. Krus-tok, and R. Stern. Ferromagnetism in rare earth doped cerium oxide bulk samples. *Phys. Status Solidi A*, 209:353, 2012.

[164] V. Fernandes, R. J. O. Mossanek, P. Schio, J. J. Klein, A. J. A. de Oliveira, W. A. Ortiz, N. Mattoso, J. Varalda, W. H. Schreiner, M. Abbate, and D. H. Mosca. Dilute-defect magnetism: Origin of magnetism in nanocrystalline CeO$_2$. *Phys. Rev. B*, 80:035202, 2009.

[165] Y. Q. Song, H. W. Zhang, Q. Y. Wen, Hao Zhu, and J. Q. Xiao. Co doping effect on the magnetic properties of CeO$_2$ films on Si(111) substrates. *J. Appl. Phys.*, 102:043912, 2007.

[166] X. Han, J. Lee, and H. I. Yoo. Oxygen-vacancy-induced ferromagnetism in CeO$_2$ from first principles. *Phys. Rev. B*, 79:100403, 2009.

[167] H. Wilkens, O. Schuckmann, R. Oelke, S. Gevers, A. Schaefer, M. Bäumer, M. H. Zoellner, T. Schroeder, and J. Wollschläger. Stabilization of the ceria ι-phase (Ce$_7$O$_{12}$) surface on Si(111). *Appl. Phys. Lett.*, 102:111602, 2013.

[168] F. Bertram, C. Deiter, K. Pflaum, and O. H. Seeck. A compact high vacuum heating chamber for *in-situ* x-ray scattering studies. *Rev. Sci. Instrum.*, 83:083904, 2012.

[169] J.P. Holgado, G. Munuera, J.P. Espinós, and A.R. González-Elipe. XPS study of oxi-dation processes of CeO$_x$ defective layers. *Appl. Surf. Sci.*, 158:164, 2000.

[170] D.R. Mullins, S.H. Overbury, and D.R. Huntley. Electron spectroscopy of single crystal and polycrystalline cerium oxide surfaces. *Surf. Sci.*, 409:307, 1998.

[171] W. Xiao, Q. Guo, and E.G. Wang. Transformation of CeO$_2$(111) to Ce$_2$O$_3$(0001) films. *Chem. Phys. Lett.*, 368:527, 2003.

[172] E. Paparazzo, G. M. Ingo, and N. Zacchetti. X-ray induced reduction effects at CeO$_2$ surfaces: An x-ray photoelectron spectroscopy study. *J. Vac. Sci. Technol. A*, 9:1416, 1991.

[173] A. Allahgholi, J. I. Flege, S. Thiess, W. Drube, and J. Falta. in preparation. 2013.

[174] J. C. Fuggle, F. U. Hillebrecht, Z. Zolnierek, R. Lässer, Ch. Freiburg, O. Gunnarsson, and K. Schönhammer. Electronic structure of Ce and its intermetallic compounds. *Phys. Rev. B*, 27:7330, 1983.

[175] E. Wuilloud, H. R. Moser, W.-D. Schneider, and Y. Baer. Electronic structure of γ- and α-Ce. *Phys. Rev. B*, 28:7354, 1983.

[176] G. Praline, B. E. Koel, R. L. Hance, H.-I Lee, and J. M. White. X-ray photoelectron study of the reaction of oxygen with cerium. *J. Electron Spectrosc. Relat. Phenom.*, 21:17, 1980.

[177] A. Laachir, V. Perrichon, A. Badri, J. Lamotte, E. Catherine, J. C. Lavalley, J. El Fallah, L. Hilaire, F. Le Normand, E. Quéméré, G. N. Sauvion, and O. Touret. Reduction of CeO_2 by hydrogen. Magnetic susceptibility and Fourier-transform infrared, ultraviolet and X-ray photoelectron spectroscopy measurements. *J. Chem. Soc. Faraday Trans.*, 97:1601, 1991.

[178] R. Olbrich, H. H. Pieper, R. Oelke, H. Wilkens, J. Wollschläger, M. H. Zoellner, T. Schroeder, and M. Reichling. in preparation. 2013.

[179] I. Manke, H. J. Wen, A. Bauer, M. Dähne-Prietsch, and G. Kaindl. Formation of the $CeSi_x$/Si(111) interface. *J. Vac. Sci. Technol. B*, 13:1657, 1995.

[180] A. Fujimori, J. J. Grioni, M. Joyce, and J. H. Weaver. Chemical bonding in ordered Ce overlayers on Si(111). *Phys. Rev. B*, 36:1075, 1987.

[181] M. Henzler. Measurement of surface defects by low-energy electron diffraction. *Appl. Phys. A*, 34:205, 1984.

[182] M. Henzler. Capabilities of LEED for defect analysis. *Surf. Rev. Lett.*, 4:489, 1997.

[183] S. Torbrügge, M. Cranney, and M. Reichling. Morphology of step structures on CeO_2(111). *Appl. Phys. Lett.*, 93:073112, 2008.

[184] V. Kanchana, G. Vaitheeswaran, A. Svane, and A. Delin. First-principles study of elastic properties of CeO_2, ThO_2 and PoO_2. *J. Phys.: Condens. Matter*, 18:9615, 2006.

[185] J. L. F. Da Silva. Stability of the Ce_2O_3 phases: A DFT+U investigation. *Phys. Rev. B*, 76:193108, 2007.

[186] H. Bärnighausen and G. Schiller. The crystal structure of A-Ce_2O_3. *J. Less-Common Met.*, 110:385, 1985.

List of Figures

List of figures

Acknowledgement

Acknowledgement